Department of Physics and Astronomy
Heidelberg University

Bachelor Thesis in Physics
submitted by

Nisa Kassandra Wöll

born in Gießen (Germany)

2023

Free-Space UV Laser-to-Waveguide Coupling

This Bachelor Thesis has been carried out by Nisa Wöll at the
Kirchhoff-Institute for Physics in Heidelberg
under the supervision of
Prof. Dr. Wolfram Pernice

Abstract

In Quantum computers, integrated photonic devices allow for scalable, high precision control of laser pulses for addressing individual qubits. In this thesis, a setup is proposed and build for the characterisation of integrated electro-optical modulator circuits. The primary function is the coupling of a free-space laser at a wavelength of 317nm into and out of an integrated control module. Using the theoretical concept of a Gaussian beam, the propagation of a laser in free-space is predicted in order to choose suitable optical components for the setup. The parameters determining the propagation of the used laser are measured in means of the knife-edge method. The efficiency of the used components is determined. A technique for coupling the laser beam into and out of an integrated waveguide is derived and explained. The influence of the polarisation of the coupled light and the waveguide width on the coupling efficiency is studied. Finally, the amount of power transmitted through a S bend waveguide of 20μm width and 200nm height is measured, revealing a coupling efficiency of 24dB.

Zusammenfassung

In Quantencomputern dienen integrierte optische Systeme der skalierbaren und präzisen Adressierung individueller Qubits durch lokale Laserpulse. In dieser Thesis wird ein optischer Freistrahl-Aufbau vorgestellt und umgesetzt, dessen Aufgabe die Charakterisierung integrierter Elektro-optischer Modulator Schaltungen ist. Die primäre Funktion des Aufbaus besteht darin, das Licht eines Freistrahl-Lasers der Wellenlänge 317nm in ein integriertes Kontrollmodul ein- und wieder auszukoppeln. Unter Ausnutzung des theoretischen Konzepts eines Gauß-Strahls wird die Propagation eines Lasers im freien Raum vorausgesagt, um die passenden optischen Komponenten auszusuchen. Die Propagations-bestimmenden Parameter des verwendeten Lasers werden durch die knife-edge Methode vermessen. Die Effizienz der verwendeten optischen Komponenten wird bestimmt. Eine Methode für das Ein- und Auskoppeln des Freistrahls in einen integrierten Wellenleiter wird ermittelt und erklärt. Der Einfluss der Polarisation des eingekoppelten Lichts und der Breite des Wellenleiters auf die Kopplungs-Effizienz wird untersucht. Zuletzt wird die durch einen S-förmigen Wellenleiter von 20μm Breite und 200nm Höhe transmittierte optische Leistung gemessen, welche einer Kopplungs-Effizienz von 24dB entspricht.

Contents

1 Introduction

Despite the steady increase in computing power, many relevant problems in science and economics elude efficient calculation. This includes a wide variety of optimisation tasks in logistics, but also the simulation of complex physical systems, such as molecules or solids [5]. Quantum computers promise an enormous increase in performance by exploiting quantum mechanical properties. Similar to classical computers, they possess a processor, performing operations and calculations to achieve a result. In a quantum computer, the unit of information is a *qubit*, the quantum equivalent of a bit. The quantum nature of qubits allows for a superposition of the two logical basis states of a single qubit [14]. Hence, a quantum computer is able to solve several problems exponentially faster and with a higher efficiency, than any modern classical computer [2].

A qubit can be encoded, for example, in a neutral atom. Multiple neutral atoms can be entangled by coupling to highly excited Rydberg states, whose electrons are located far from the nucleus, allowing for long-range dipole-dipole interactions of the neutral atom qubits [4]. Thus, one- or more-qubit quantum gates can be realised. The individual qubits can be addressed in means of local laser beams. To precisely control a large number of qubits, an integrated photonic device is chosen as a control unit of the beams, guaranteeing a scalable quantum computer.

Integrated photonics refers to the technology and research concerned with the integration and miniaturisation of various passive and active optical components on a single substrate, the *chip*, interconnected via small optical transmission lines, the *waveguides* [10]. Similar to conventional electronics, the integration of optical components onto a chip allows for the creation of complex and functional circuits, using photons instead of electrons. One of the fundamental building blocks in integrated photonic circuits is a waveguide-integrated electro-optic phase modulator. This device can serve as an optical switch by controlling the phase of the guided light to create constructive or destructive interference [12].

Within the frame of the Munich Quantum Valley Initiative, the consortium MUNICQ ATOMS has the aim of realising a neutral atom based quantum processor with up to 400 qubits encoded in Strontium atoms [9]. The research team under the supervision of Professor Wolfram Pernice at the University of Heidelberg is responsible for building integrated optical switches for high precision single atom addressing. In order to realise two-qubit gates by coupling to Rydberg states, the aspired wavelength of the photons lies in the ultraviolet (UV) range at 316nm, corresponding to the electronic transition $^3P_0 \rightarrow {}^3S_1$ within a Strontium atom. In an integrated photonic circuit, a suitable waveguide material for this wavelength is Aluminium Gallium Nitride, which has a large band-gap in the UV regime.
This thesis presents a setup for the characterisation of integrated electro-optical modulator circuits controlling light in the UV range. The core of the setup is the coupling of a free-space laser at 317nm wavelength into and out of an integrated waveguide. The light beam is coupled into the waveguide, by directly focusing it at one end. To ensure a high coupling efficiency, a precise alignment mechanism is incorporated. This includes a two-part monitoring system of the coupled waveguide. The choice of a free-space setup offers advantages in comparison to a conventional fiber approach at wavelengths in the UV regime. The highly energetic photons cause photothermal damage to the fiber material, resulting in degradation effects and the occurrence of defects [7]. Hence, a fiber must be changed regularly. On the contrary, the optical components in a free-space setup allow for long testing periods during the process of finding the right chip design and fabrication technique. Additionally, a free-space setup allows for greater flexibility in reconfiguring the setup. However, the choice of a free-space setup also bears some difficulties. The beam path excludes the use of a commercial microscope for imaging the end of the coupled waveguide. Furthermore, the coupling efficiency is limited by the spot size achievable in means of state-of-the-art objective lenses. This efficiency is additionally limited by the quality of the used laser beam.

2 Theoretical Framework

This chapter introduces the underlying theoretical principles for this thesis. Section 2.1 discusses the propagation of a single-mode laser beam in free-space and its transmission through different optical components while using the concept of a Gaussian beam. This theoretical concept is subsequently generalised for real laser beams in section 2.1.5. To characterise an integrated photonic device, light is coupled into the integrated waveguide. Section 2.2 discusses the basic principles of waveguide theory and introduces a method for coupling a free-space beam to a waveguide. As part of a monitoring system, structures on a sub-micrometre scale must be studied. Section 2.3 depicts the important components and function of an infinity-optical microscope, as used in the setup.

2.1 The Gaussian Beam

Although laser sources emit a light beam with a low degree of angular spread, the wave nature of light excludes a spatially confined transport in free-space. Under ideal circumstances, however, the light of a single-mode laser takes the form of a so-called *Gaussian beam* while propagating in free-space. This type of beam, as this section describes, comes as close as possible to a spatially localised and non-diverging beam. The word 'Gaussian' refers to the cross-section of the beam, which exhibits a profile according to a circularly symmetric Gaussian distribution with a width varying along the axis of propagation, the *optical axis*. In practice, the Gaussian beam is the simplest and often the most desirable type of beam provided by a laser, as it is well characterised and its evolution can be predicted with ease.

2.1.1 Complex Amplitude

In free-space, light propagates in the form of electromagnetic waves. The optical wave is mathematically described by a real function of the position $\mathbf{r} = (\mathrm{x,y,z})^T$ and time t, called the *wavefunction* $u(\mathbf{r}, t) \in \mathbb{R}$. This function is often represented by a complex function $U(\mathbf{r}, t)$, with $u(\mathbf{r}, t) = Re\big(U(\mathbf{r}, t)\big)$, referred to as the *complex wavefunction*. Both functions satisfy the same boundary conditions and the well-known wave equation $\Delta u - \frac{1}{c^2}\partial_t^2 u = 0$. For a monochromatic wave of the wavelength

λ, the complex wavefunction is given by

$$U(\mathbf{r},t) = a(\mathbf{r})\, exp\big(i\varphi(\mathbf{r})\big)\, exp\big(i\, 2\pi\nu t\big) = U(\mathbf{r})\, exp\big(i\, 2\pi\nu t\big)\,, \tag{2.1}$$

with the phase $\varphi(\mathbf{r})$, the frequency ν, the amplitude a($\mathbf{r}$) and the *complex amplitude* $U(\mathbf{r})$ of the wave.
By substituting the complex wavefunction into the wave equation, a different form of this equation, the *Helmholtz equation* is obtained

$$(\Delta + k^2)U(\mathbf{r}) = 0\,, \tag{2.2}$$

with the *wavenumber* $k = \frac{2\pi\nu}{c} = \frac{2\pi}{\lambda}$, according to the dispersion relation.
In an optical system, electromagnetic waves ideally propagate in the form of paraxial waves. Paraxial waves possess wavefront normals corresponding to paraxial rays, that by definition always enclose a small angle with the optical axis and remain close to this axis throughout the system. A paraxial wave is described by a plane wave e^{-ikz}, propagating along the optical axis and modulated by a complex envelope $A(\mathbf{r})$, that is slowly varying in respect to the optical axis. The envelope is considered constant within an environment of the size λ. For paraxial waves equation 2.2 simplifies to the *paraxial Helmholtz equation*. By inserting $U(\mathbf{r}) = A(\mathbf{r})exp(-ikz)$ into equation 2.2 and using the assumption of paraxial waves, the paraxial Helmholtz equation follows as

$$(\Delta_T - 2ik\,\partial_z)A(\mathbf{r}) = 0\,, \tag{2.3}$$

with the transverse part of the Laplacian operator $\Delta_T = \partial_x^2 + \partial_y^2$.
The complex envelope of a paraxial wave results from the paraxial Helmholtz-equation

$$A(\mathbf{r}) = \frac{A_1}{q(z)}\, exp\big(-ik\frac{\rho^2}{2q(z)}\big)\,, \qquad \rho^2 = x^2 + y^2 \quad A_1 \in \mathbb{R}\,, \tag{2.4}$$

with a function $q(z) = z - a$, where a is an arbitrary constant.
If the constant a is real, the solution provides a paraboloidal wave, centred around the point $z = a$ on the optical axis. If a is solely imaginary, e.g., $a = -iz_R$ ($z_R \in \mathbb{R}$), equation 2.4 still provides a valid solution to the paraxial Helmholtz equation and gives rise to the complex envelope of a Gaussian beam.
The complex amplitude of a Gaussian beam is derived from its complex envelope by separating the amplitude and phase via inserting $\frac{1}{q(z)} = \frac{1}{R(z)} - i\frac{\lambda}{\pi W^2(z)}$, with the

two real functions $W(z)$ and $R(z)$ and the constant $a = -iz_R$

$$U(\mathbf{r}) = A_0 \frac{W_0}{W(z)} exp\big(-\frac{\rho^2}{W^2(z)}\big) exp\big(-i(kz + k\frac{\rho^2}{2R(z)} - \eta(z))\big)\,, \tag{2.5}$$

with the parameters

$$W(z) = W_0\big(1 + (\frac{z}{z_R})^2\big)^{1/2} \tag{2.6}$$

$$R(z) = z\big(1 + (\frac{z_R}{z})^2\big) \tag{2.7}$$

$$\eta(z) = tan^{-1}\frac{z}{z_R} \tag{2.8}$$

$$W_0 = \big(\frac{\lambda z_R}{\pi}\big)^{1/2} \tag{2.9}$$

$$A_0 = \frac{A_1}{iz_R}\,, \qquad A_1 \in \mathbb{R}\,. \tag{2.10}$$

The real constant z_R is commonly referred to as the *Rayleigh range*. The following subsection will reveal the meaning of the functions $R(z)$, $W(z)$ and $\eta(z)$ alongside the important properties of a Gaussian beam.

2.1.2 Properties

The optical intensity of a Gaussian wave is calculated from the complex amplitude according to $I(\mathbf{r}) = |U(\mathbf{r})|^2$ and, thus, results in

$$I(\mathbf{r}) = I_0\big(\frac{W_0}{W(z)}\big)^2 exp\big(-\frac{2\rho^2}{W^2(z)}\big)\,, \qquad I_0 = |A_0|^2\,. \tag{2.11}$$

This corresponds to a Gaussian distribution in dependence of the radial distance ρ, centred around the optical axis with a standard deviation of $\sigma = \frac{1}{2}W(z)$ for every position on the optical axis. The maximum Intensity I_0 is reached in the beam centre for the axial distance $z = 0$. Figure 2.1 shows the normalised radial intensity distribution $I(\rho)/I_0$ for the axial distance $z = 0$ alongside the expected beam profile. For any transverse plane, the total optical power carried by the beam is given by

$$P = \int_0^\infty \int_0^{2\pi} I(\rho, z)\rho \, d\rho \, d\varphi = \frac{\pi}{2} I_0 W_0^2\,. \tag{2.12}$$

As expected, the result is independent of the position on the optical axis, as ideally no power is lost when propagating through space.

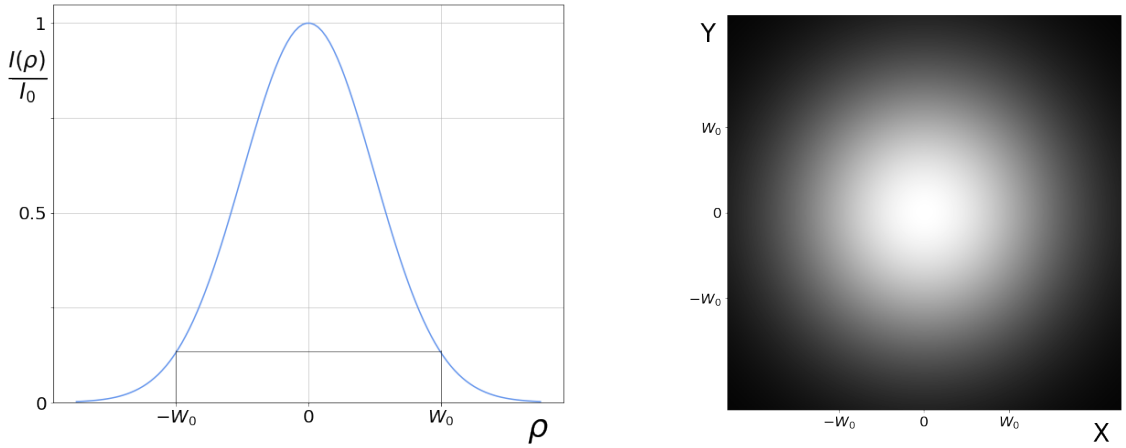

Figure 2.1: Normalised intensity distribution I/I_0 of a Gaussian beam as a function of the radial distance ρ at the axial distance $z = 0$.

The intensity drops by the factor $1/e^2 \approx 0.135$ from its maximum value at the radial distance $\rho = W(z)$ for any position on the optical axis. Thus, the function $W(z)$ is referred to as the *radius* of the Gaussian beam. According to equation 2.6, the radius reaches its minimum value W_0 for $z = 0$. This value, which governs the beam evolution, is known as the *beam waist* or *focus*. Starting from the waist, the beam radius increases in both directions along the optical axis. Within the so-called *depth of focus*, the radius lies within a factor of $\sqrt{2}$ of the waist radius and can still be considered as in focus. According to equation 2.6, this range equals to two times the Rayleigh range.
Far from the beam waist ($z \gg z_R$) the expression 2.6 simplifies to

$$W(z) \approx \frac{W_0}{z_R} z = \theta_0 z \,. \tag{2.13}$$

Hence, for great axial distances the beam can be approximated as a cone with half-angle θ_0, commonly referred to as the *divergence* of the beam. Using equation 2.9 and 2.13 the divergence is defined as

$$\theta_0 = \frac{\lambda}{\pi W_0} \,. \tag{2.14}$$

Figure 2.2 shows a plot of the beam radius $W(z)$, with the approximation for great axial distances indicated.

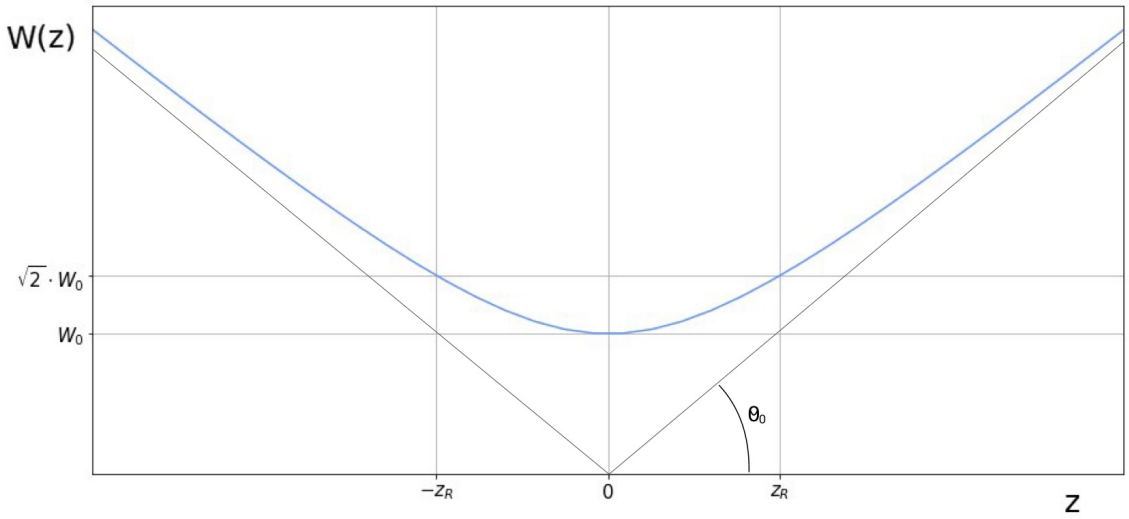

Figure 2.2: Radius of a Gaussian beam as a function of the axial distance z.

The phase of the Gaussian wave is, according to equation 2.5, composed of three components

$$\varphi(z) = kz - \eta(z) + k\frac{\rho^2}{2R(z)}. \tag{2.15}$$

The component kz corresponds to the phase of a plane wave. The second component represents a phase retardation $\eta(z)$ reaching from $-\frac{\pi}{2}$ for z=-∞ to $\frac{\pi}{2}$ for z=∞ (equation 2.8). This π phase shift when the light wave passes through its focus, is known as the *Guoy effect* with the *Guoy phase* η(z) and resembles an excess delay of the wavefronts in comparison to a plane or spherical wave. The third component of the phase corresponds to a bending of the wavefronts.

The wavefronts are defined as surfaces of constant phase, satisfying φ(z)=2πq with an arbitrary integer q. For a Gaussian beam, the wavefronts correspond to paraboloidal wavefronts for every position of the optical axis with the radius of curvature $R(z)$. Thus, $R(z)$ is commonly referred to as the radius of curvature of the wavefront located at the axial distance z. The radii are positive for convex and negative for concave wavefronts.

In total, the Gaussian beam is fully described by four parameters, the amplitude, the optical axis, the position of the waist and the waist radius.

Assuming that the beam radius W and the radius of curvature R of a Gaussian beam are known at some point on the optical axis, the waist radius W_0 and the

position $z = s$ of the waist can be calculated according to

$$W_0 = \frac{W}{\sqrt{1 + (\pi W^2/\lambda R)^2}} \tag{2.16}$$

$$s = -\frac{R}{1 + (\lambda R/\pi W^2)^2}\,. \tag{2.17}$$

2.1.3 Transmission through a thin Lens

The properties of a Gaussian beam are altered by a lens. A thin biconvex lens is described by two plano-convex lenses, with radii R_1 and R_2, facing away from each other. In the approximation of paraxial rays ($x^2 + y^2 \ll R_i^2$), the profile of a plano-convex lens is mathematically expressed by

$$d_i(x, y) = \pm(d_i - \frac{x^2 + y^2}{2R_i}), \qquad i = 1, 2\,, \tag{2.18}$$

where d_i denotes the thickness of each plano-convex lens. By convention, $R_1 > 0$ and $R_2 < 0$ applies for the convex and concave lens-surfaces.
The transmittance $t(x, y) = \frac{U(x,y,z+d_i)}{U(x,y,z)}$ of a Gaussian beam with the wavenumber k through a plano-convex lens is given as the product of the transmittance through a layer of air (refractive index $n_0 \approx 1$) of the thickness $d_i - d_i(x, y)$ and a layer of the lens material ($n_{lens} = n$) of the thickness $d_i(x, y)$ according to

$$t(x, y) \approx exp\big(-ikd_i\big)\, exp\big(-i(n-1)kd_i(x, y)\big)\,. \tag{2.19}$$

Hence, the transmittance through a thin biconvex lens of the thickness $d_0 = d_1 + d_2$ is given by the product of the transmittance through each plano-convex lens

$$t(x, y) = exp\big(-ikd_0\big)\, exp\big(ik\frac{x^2 + y^2}{2f}\big)\,, \tag{2.20}$$

with the *focal length* f, defined as

$$\frac{1}{f} = (n-1)\big(\frac{1}{R_1} - \frac{1}{R_2}\big), \tag{2.21}$$

which is consistent with the Lensmaker's equation for a thin lens ($d_0 \ll R_1, R_2$).
The transmission of a Gaussian beam through a thin lens, thus, results in an altered

phase according to

$$\varphi'(z) = kz + k\frac{\rho^2}{2R} - \eta(z) - k\frac{\rho^2}{2f} = kz + k\frac{\rho^2}{2R'} - \eta(z)\,. \tag{2.22}$$

Based on the right side of equation 2.22, it is concluded that the transmitted beam

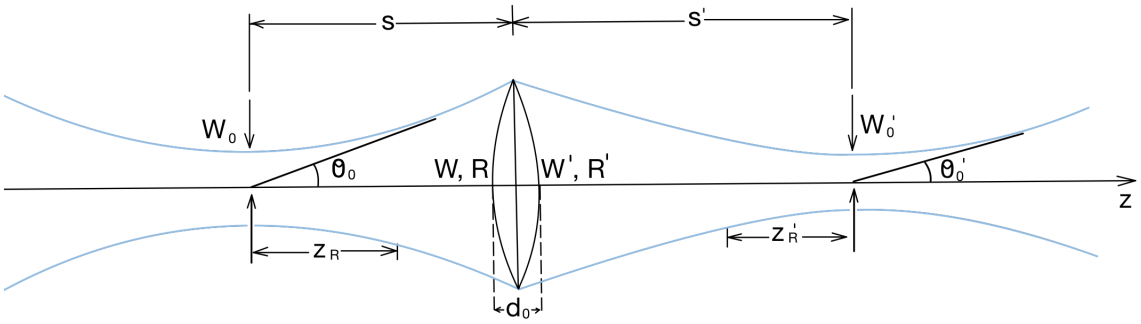

Figure 2.3: Propagation of a Gaussian beam through a thin lens.

still is a Gaussian beam. At the position of the lens, the transmitted beam has the same radius $W' = W$, but a changed radius of curvature R', according to $\frac{1}{f} = \frac{1}{R} - \frac{1}{R'}$. Here, R is positive as the incident beam is diverging, whereas R' is negative as the transmitted beam is converging. The waist radius and position of the altered beam is calculated from the altered radius of curvature and the beam radius at the position of the lens according to equations 2.16 and 2.17.

2.1.4 Beam Shaping

Altering the properties of a Gaussian beam is commonly referred to as *beam shaping*. Two ways of shaping the beam, which are used in the setup, are beam focusing and beam expansion.

Beam Focusing

A lens or an objective is used to reach a smaller waist radius and, hence, a smaller spot size $D = 2W_0$ of the beam. For a thin biconvex lens placed in the beam path of a sufficiently collimated beam with a depth of focus much longer than the focal length, the lens position can be approximated as the position of the beam waist.

In this approximation, equations 2.16 and 2.17 simplify to

$$W_0' \approx \frac{\lambda}{\pi W_0} f = \theta_0 f \tag{2.23}$$

$$s' \approx f\,. \tag{2.24}$$

Hence, the waist of the focused beam is located directly at the focal point of the lens. According to equation 2.23, the altered waist radius is inversely proportional to the incident waist radius. Thus, the smallest spot size for a specific wavelength is reached for a large waist radius and a small divergence of the incident beam.

Beam Expansion

A Gaussian beam is expanded and collimated by a so-called *Kepler telescope* consisting of two lenses with focal lengths f_1 and f_2, that satisfy $f_1 < f_2$. Figure 2.4 shows the scheme of a Kepler telescope.

The first lens, which has a short focal length, focuses the incident beam to a smaller waist radius located at a distance s_1. The second lens, which has a long focal length,

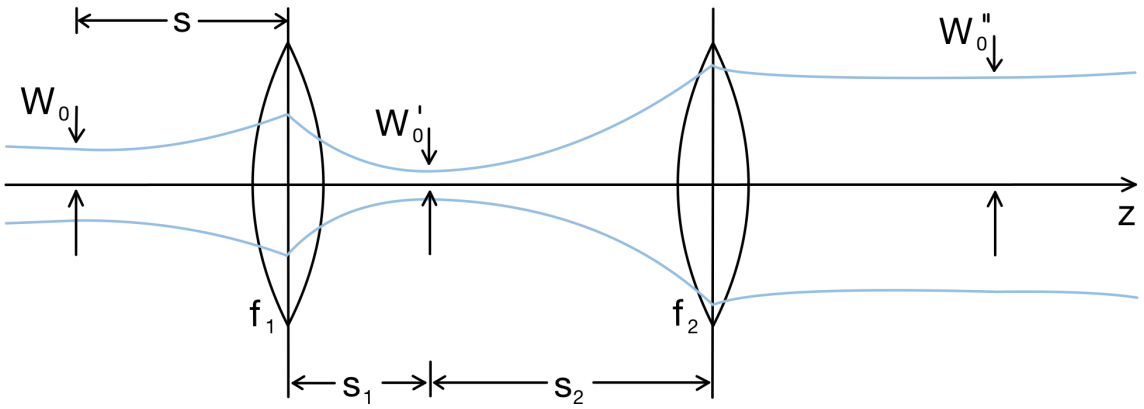

Figure 2.4: Beam expansion in means of a Kepler telescope.

expands the waist radius. The expanded waist radius W_0'' becomes maximum, if the distance s_2 between the second lens and the intermediate waist W_0' coincides with its back focal length f_2, corresponding to

$$W_0'' = W_0 \frac{f_2}{f_1} \sqrt{\left((s - f_1)^2 + z_R^2\right)/z_R^2}\,. \tag{2.25}$$

By assuming that the first lens is placed, so that the incident waist position coincides with its back focal point $s \approx f_1$, the geometrically expected result is obtained

$$W_0'' = W_0 \frac{f_2}{f_1} \qquad \text{with } s = f_1 \,. \tag{2.26}$$

As the Rayleigh range is directly proportional to the waist radius, the beam expansion results in an expanded depth of focus, corresponding to a higher collimation of the beam.

2.1.5 Real Beam Propagation

Although the output beam of a real-life single-mode laser comes as close as possible to the theory of a Gaussian beam, still deviations can occur for real laser sources. The deviations can be attributed to factors, such as the oscillation of higher-order transverse modes, amplitude and phase distortions caused by an inhomogeneous gain distribution in the laser medium or the formation and superposition of partial beams [3]. A factor M^2, typically referred to as the *beam propagation factor*, was established to describe such non-Gaussian beams.
To quantify the quality of a laser beam, the property is used that for any given laser beam the so-called *beam parameter product* $BPP = \theta_0 \cdot W_0 = \lambda/\pi$ remains constant while propagating through space. The mentioned reasons for a deviation

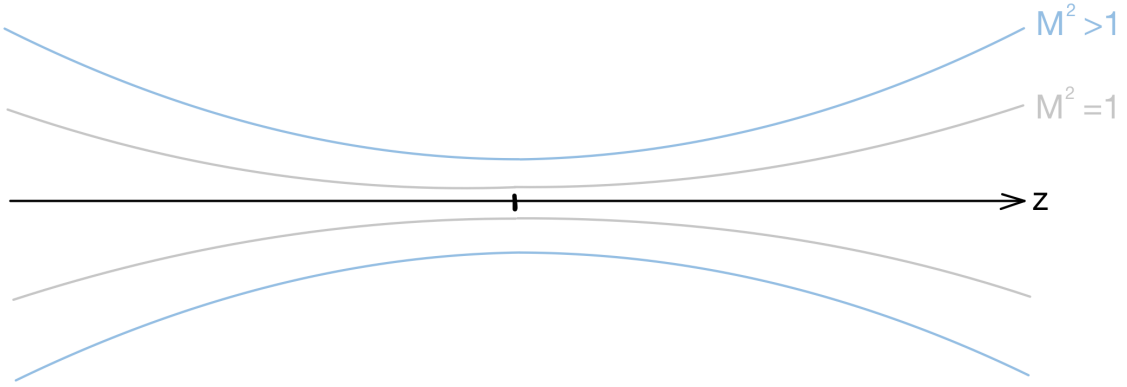

Figure 2.5: Deviation of a real laser beam from the theoretical Gaussian beam.

of real laser beams from the Gaussian theory lead to an increase of both, the waist radius and the divergence by a factor of M. The beam propagation factor is defined as

$$M^2 = \frac{\theta_{0,r} W_{0,r}}{\theta_0 W_0} = \theta_{0,r} W_{0,r} \frac{\pi}{\lambda} \,, \tag{2.27}$$

with the parameters $\theta_{0,r}$ and $W_{0,r}$ corresponding to the real beam.
The factor is minimal for a theoretical Gaussian beam with $M^2 = 1$ and larger for real laser beams $M^2 > 1$. Figure 2.5 illustrates the deviation of a real beam from the theoretical Gaussian, while assuming the same waist position for both.
The deviation of a real beam from the theoretical Gaussian beam is considered by including it in calculations, according to the former results.

2.2 Coupling to optical Waveguides

A waveguide is a structure allowing the confinement of light within its boundaries by means of total internal reflection [8]. It is the basic element in integrated photonics technology, as it serves as a connection between different optical components on a chip. A waveguide consists of a dielectric material, the *core*, surrounded by another dielectric material of lower refractive index $n_2 < n_1$, the *cladding*, granting total internal reflection at the interface.
Within a waveguide, light propagates in the form of *modes*, fields that maintain the same transverse distribution and polarisation at all points of the waveguide axis. An in-detail wave analysis of waveguides exceeds the scope of this thesis. A fundamental study may be found in the referenced sources [3, 12, 15]. This section outlines the underlying theory for coupling a free-space laser beam into a channel waveguide, which confines light in two directions.

2.2.1 Excitation of Modes

In a first approximation, a channel waveguide is assumed a loss-less structure with a transverse distribution according to a rectangle, which is invariant in the direction of propagation, say the z-direction. The electromagnetic field of the modes in a waveguide structure form a complete system of orthogonal functions [8]. Thus, the complex amplitude of an arbitrary electromagnetic field, propagating in a waveguide can in principle be written as the weighted superposition of the modes of the waveguide

$$\mathbf{E}(x,y,z) = \sum_m a_m \mathbf{u}_m(x,y) e^{-i\beta_m z} \tag{2.28}$$

$$\mathbf{H}(x,y,z) = \sum_m a_m \mathbf{v}(x,y) e^{-i\beta_m z}\,. \tag{2.29}$$

Here, a_m denotes the amplitude, $\mathbf{u}_m(x, y)$ the transverse distribution and β_m the propagation constant of the m-th mode. The latter corresponds to the projection of the wavevector of the guided light onto the waveguide axis. Utilising Maxwell equations, the spatial distribution and the amplitude can be determined for each mode.

To excite one of the modes of the waveguide, the coupled light must have a similar transverse distribution and polarisation as said mode. For an arbitrary distribution $\mathbf{s}$(x,y) of the coupled light, different modes are excited by different amounts. The amount of power transmitted to one of the modes depends on the overlap of the distribution of light $\mathbf{s}$(x,y) and that of the mode $\mathbf{u}_m(x, y)$. The distribution of the incident light can be written as an expansion of the functions $\mathbf{u}_m(x, y)$

$$\mathbf{s}(x, y) = \sum_m b_m \mathbf{u}_m(x, y)\,, \tag{2.30}$$

with the amplitude $\mathbf{b}_l$ of the excited mode l

$$b_l = \int_{-\infty}^{\infty} \mathbf{s}^*(x, y) \cdot \mathbf{u}_l(x, y) dx\, dy\,. \tag{2.31}$$

2.2.2 Free-Space Laser-to-Waveguide Coupling

To couple the light of a free-space laser to a waveguide, the beam is shaped, so that its transverse distribution becomes similar to the transverse distribution of the modes of the waveguide. Hence, the beam is focused to a spot size close to the dimension of the waveguide. In order to focus the beam onto a particularly small spot, it is advantageous to use an infinity-corrected objective, which focuses a collimated beam path with a diminished level of aberrations in comparison to a simple lens [12]. The coupling efficiency becomes maximum for a spot size equal to or smaller than the dimension of the waveguide.

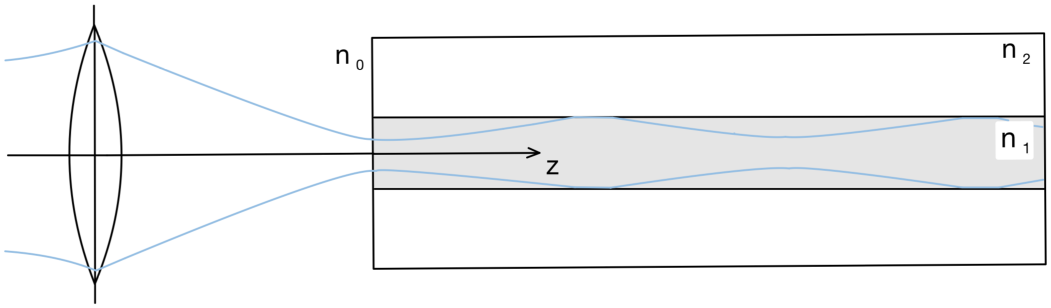

Figure 2.6: Coupling a free-space laser into a waveguide.

2.3 Infinity-corrected Microscopes

Microscopes enable the examination of structures the bare human eye is unable to resolve. In a classical microscope the objective creates a non-parallel beam path between the objective and ocular lens, precluding the inclusion of additional optical elements, such as polarisers or beamsplitters, without the occurrence of unwanted aberrations. In response to this problem, *infinity-optical systems* have been developed, where special infinity-corrected objectives enable a collimated beam path between the objective and the so-called *tube lens*. An infinity-corrected objective

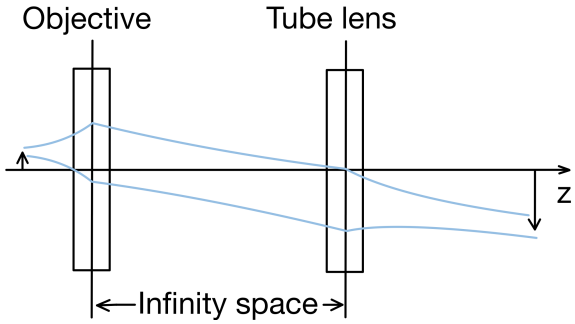

Figure 2.7: Scheme of an infinity-corrected microscope.

projects the image of the specimen into infinity. Hence, the beam leaving the objective is collimated. The collimated beam is subsequently focused by a tube lens, forming a magnified, upside-down intermediate image. By placing a camera at this intermediate image, the specimen can be observed. Additional optical elements can be placed within the parallel beam path between the objective and the tube lens, the so-called *infinity space*, without creating additional aberrations.

3 Experimental Setup

This chapter introduces the experimental setup for coupling a free-space laser in the UV regime to an integrated waveguide. Section 3.1 explains the concept of the setup. Subsequently, section 3.2 discusses the choice of components alongside their important specifications. To choose the correct components, the laser beam is characterised. Section 3.3 explains the used techniques of measurement.

3.1 Concept

To characterise integrated photonic circuits, monochromatic light of a suitable wavelength and spatial distribution must be efficiently coupled into and out of the integrated waveguide. The free-space setup, proposed and built during this thesis, characterises integrated control modules operating at a wavelength of 316nm. Figure 3.1 shows a scheme of the setup.
The monochromatic light of the laser enters the setup in the upper right corner. A combination of mirrors corrects the height and direction of the beam. In order

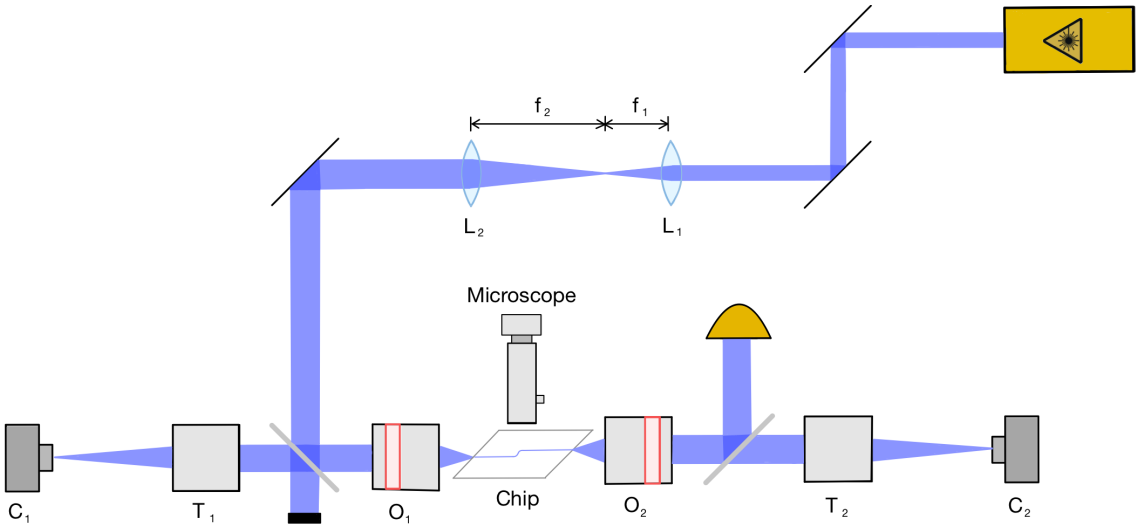

Figure 3.1: Scheme of the free-space UV laser-to-waveguide coupling setup, with L_1, L_2: Simple lens with focal length f_1, f_2, satisfying $f_1 < f_2$, O_1, O_2: Infinity-corrected objective, T_1, T_2: Tube-lens, C_1, C_2: Camera.

to couple the free-space beam to a waveguide, it is shaped first. The light of a

free-space laser is coupled into the waveguide by directly focusing it at one end. For this sake, an infinity-corrected objective O_1 is used, focusing the beam to a spot size close to the dimension of the waveguides facet. To reach the small spot size, the used objective requires a sufficiently large diameter of the incident beam. As the output beam of the laser initially exhibits a beam radius below the requirement, the beam diameter is expanded in means of a Kepler telescope first. This telescope is formed by the two lenses L_1 and L_2, satisfying $f_1 < f_2$.

To precisely align the waveguides facet with the waist of the focused beam, the chip is mounted on a combination of motorised stages. As the dimension of a waveguide prohibits an alignment by eye, a two-part monitoring system is included in the setup. First, the top surface of the chip is examined using a commercial microscope setup. Once light has been successfully coupled to the waveguide, losses at the surface of the waveguide are monitored in means of this microscope. The higher the coupling efficiency is, the more losses are observed. Second, the objective O_1, used for coupling into the waveguide, simultaneously serves as the objective of an infinity-corrected microscope, consisting of an additional tube lens T_1 and the camera C_1. Light that is reflected from the side surface of the chip back into the objective is observed in means of the camera. Thus, the correctness of the height of the chip and the objective-facet distance can be verified. In order to simultaneously couple light into the waveguide and observe the reflections from the side of the chip, a beamsplitter is placed within the infinity space of this microscope setup.

Once light has been successfully coupled into the waveguide, the transmitted light can be analysed. This light is collected and collimated in means of a second infinity-corrected objective O_2, placed at the back end of the waveguide. This objective is also part of an infinity-corrected microscope, formed by the tube lens T_2 and the camera C_2 and containing a beamsplitter that guides a fraction of the beam out of the microscope again. The microscope setup is mounted on a translation stage, allowing movements along three axes for aligning the objective with the back end of the waveguide. Light passing the beamsplitter towards the camera serves as an indicator for the correct position of the microscope setup.

Finally, the transmitted power is measured in means of a power meter. This devise is mounted in the reflected beam path from the beamsplitter. For different applications, it is possible to replace the power meter with a collimator, which guides the beam to a spectrometer in means of a fiber.

3.2 Choice of Components

In the setup different optical components are utilised, selected according to the properties of the laser beam. This section explains the reasons for choosing the components and lists their important specifications.

Laser Source
The utilised laser generates a maximum output power of 250mW at a wavelength of approximately 317nm, close to the aspired spectral line within a Strontium atom. In a measurement, which will be explained in more detail in section 3.3, the waist radius of this laser results in $(996 \pm 10)\mu$m (Section 4.1.2). The wavelength of this laser served as a reference for the required optical elements. This specific wavelength is generated from light lying in the infrared regime through two separate second harmonic processes in which two photons of the same frequency interact, so that a new photon of twice the initial frequency is created. The cavities of both second harmonic generators must be aligned and locked manually. As this laser is not intended for the commercial use, it exhibits a low stability.
For the coarse alignment and first tests of the setup, a fiber-coupled laser at a wavelength close to the UV range in combination with a single-mode fiber and a collimator is used. A fiber is a cylindrical shaped dielectric waveguide. Single-mode fibers are specifically designed to carry only a single mode of the coupled light. The fiber-coupled laser, hence, produces a high quality fundamental mode output beam. As this laser is built for the commercial use, it exhibits a high stability of the output power. According to the manufacturer of the laser *Thorlabs*, it generates a maximum output power of 20mW at a wavelength of approximately 405nm. The collimator creates a waist radius of $(341 \pm 6)\mu$m, as measured during the execution of this thesis (Section 4.1.1).

Guiding the Beam in Free-Space
The mirrors guiding the beam are chosen to exhibit a high reflectance in the UV range. UV-enhanced Aluminium mirrors are in use with a reflectance of approximately $R_M \approx 93\%$ at the wavelength of 317nm and $R_M \approx 92\%$ at 405nm.
As described in the previous section, beamsplitters are used to include a monitoring system in the setup. The utilised plate beamsplitters are front coated with a UV Fused Silica Substrate, showing a slight polarisation dependence. An average splitting ratio of 50:50 for unpolarised light at both wavelengths is chosen. An anti

reflective coating for wavelengths ranging from 250nm to 450nm is layered on the back surface of the beamsplitter, in order to reduce unwanted interference effects resulting from total reflection at this surface.

Beam shaping

A typical integrated channel waveguide facet exhibits a rectangular geometry on a micrometre scale. For the purpose of focusing the beam at the end of the waveguide, an infinity-corrected objective, suitable for the UV range, is chosen corresponding to a theoretical spot size of 0.7μm at a wavelength of 317nm and 0.9μm at 405nm. The objective contains lens elements with low absorption in the aspired spectral range. According to the manufacturer, the objective transmits $T_{obj} \approx 78\%$ of the incident beam at a wavelength of 317nm and $T_{obj} \approx 67\%$ at 405nm. To reach the aspired spot size, the objective requires an entrance beam radius of approximately 1.7mm. In order to expand the beam radius of the fiber-coupled laser from $W_0 = 0.341$mm to $W_0 = 1.7$mm, two lenses forming a Kepler telescope are used. According to equation 2.26, the ratio of the two focal lengths must equal $(\frac{f_2}{f_1})_{theo,\,405} = 4.99 \approx 5.0$. Hence, the first lens is chosen with a short focal length of $f_1 = 35.0mm$ and the second lens with a long focal length of $f_2 = 175.0$mm, corresponding to a ratio of $(\frac{f_2}{f_1})_{exp,\,405} \approx 5.0$. As the UV laser exhibits a different waist radius, a different set of lenses is used for the beam expansion. In this case, the ratio of the two focal lengths must equal $(\frac{f_2}{f_1})_{theo,\,317} = 1.71 \approx 1.7$. Two lenses were chosen with the focal lengths $f_1 = 75.0$mm and $f_2 = 125.0$mm, corresponding to a ratio of $(\frac{f_2}{f_1})_{exp,\,317} \approx 1.67 \approx 1.7$. The lenses are AR coated for the UV range and transmit $T_{lens} \approx 95\%$ of the incident beam at a wavelength of 317nm and $T_{lens} \approx 96\%$ at 405nm. For a precise adjustment of the distance between the lenses, one of the lenses is mounted on a translation stage. Both sets of lenses are included in the setup in means of a mirror, mounted in a flip mount.

Monitoring System

The choice of components of the infinity-corrected microscope monitoring the side surface of the chip is based on the selected objective for coupling into a waveguide. The tube lens chosen was the one recommended by the manufacturer for this objective. This tube lens-objective combination allows for a magnification of fifty times. The camera used is suitable for wavelengths ranging from 200nm to 1100nm. It contains sensors of the *CMOS* type (*Complementary metal oxide semiconductor*), which convert photons to electrons via the photoelectrical effect within each pixel.

The distances between objective, tube lens and camera must be adjusted precisely. Additionally, each component must be centred around the optical axis. Hence, the different components are mounted within a cage system, keeping the distances between the components constant and aligning them along one axis.
To monitor the top surface of the chip, a commercial microscope setup is used, allowing a magnification of up to eighteen times.

Chip
During first tests of the setup, different chips were used, containing several S bend waveguides of varying width. A S bend waveguide creates an offset of the optical axis. This way it can be verified that light has been successfully coupled into and out of the waveguide. Additionally, it can be distinguished between light, that has been coupled into the waveguide and light that is, for example, diffracted into the cladding. The chips are mounted on a motorised stage allowing movements along three axes in combination with a motorised rotation stage, corresponding to a minimum step size of 0.05μm for the translation and 0.0005° for the rotation stage. The waveguides are fabricated either from Aluminium Gallium Nitride or Silicon Nitride with a height of 300nm and 200nm, respectively. Both materials exhibit a low absorption in the UV range.

3.3 Beam Characterisation

To select suitable optics for the setup, it is necessary to know the parameters determining the propagation of the laser in free-space. There are many techniques for ascertaining the parameters. In this thesis, first, the beam profile is imaged and the corresponding intensity distribution is analysed in order to qualitatively assess the deviation of the beam from a theoretical Gaussian. The beam radius is measured for multiple positions along the optical axis in means of the so-called *knife-edge method*. To calculate the propagation determining parameters from the measured beam radii, a simulation software, called *GaussianBeam*, is used.

Imaging of the Beam Profile

To estimate the deviation of the beam cross-section from the theoretical circularly symmetric Gaussian beam, the beam profile is imaged and the corresponding intensity distribution is plotted. For this purpose, a camera is brought into the beam path. As the used cameras are not suitable for large optical powers, multiple 90:10 beamsplitter are placed in the beam path, splitting off 90% of the beam each. Additionally, an optical filter is mounted in front of the camera.

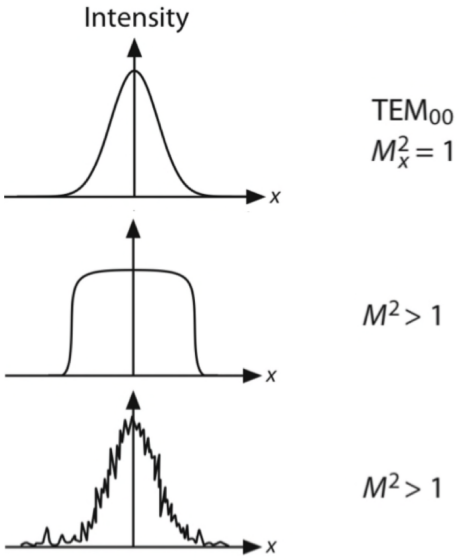

Figure 3.2: Various beam profiles and corresponding M^2 factors [3].

By analysing the plot of the intensity distribution corresponding to the imaged beam profile, the beam quality can be estimated. A high quality output beam, corresponding to a M^2 factor of approximately one, exhibits a continuous intensity distribution with only a few indents, which comes as close as possible to a Gaussian distribution. A low quality output beam, corresponding to a M^2 factor exceeding one, can show many indents throughout the intensity distribution (Figure 3.2 at the bottom) or exhibit a plateau-like area at the maximum intensity range (Figure 3.2 in the middle), similar to a flat-top beam.

Knife-Edge Method

The beam to be examined is focused by a simple lens, so that the position of the altered beam waist can be identified with ease. For different positions before and after the altered beam waist, the edge of a knife, such as a razorplate, is moved along the x axis indicated in figure 3.3, to progressively cover the beam. The transmitted power of the clipped beam is measured as a function of the knife-edge position in means of a power meter.

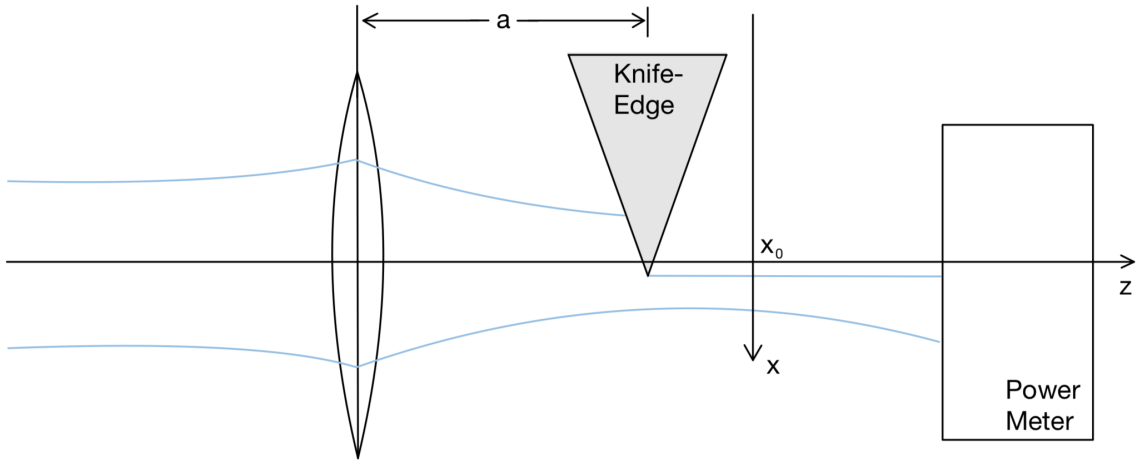

Figure 3.3: Measurement of the beam radius by knife-edge method.

A fit of the transmitted power is performed, according to

$$P(x) = \int_{-\infty}^{x-x_0} \int_{-\infty}^{\infty} I(x,y)\, dx\, dy \tag{3.1}$$

$$= P_0 + \frac{1}{2} P_{max}\big(1 - erf(\frac{\sqrt{2}(x-x_0)}{W(z)})\big)\,, \tag{3.2}$$

with the background power P_0, the unperturbed power of the beam P_{max}, the position x_0 of the knife-edge where the real measured power has halved and the standard error function $erf(z) = \frac{2}{\sqrt{\pi}} \int_0^z e^{-t^2} dt$.
For each axial distance of the knife-edge, the beam radius $W(z)$ is obtained from the fit.

Simulation of the Beam Path

The propagation determining parameters of the used laser are calculated from the results from the knife-edge method, in means of a simulation software called *GaussianBeam*. GaussianBeam is a graphical software that traces the beam path of a laser in one dimension, calculating the beam radius and radius of curvature for every position on the optical axis. The software allows to set the M^2-factor and the wavelength λ of the used laser. The propagation determining parameters, such as the waist radius and the divergence, can be simulated from a measurement of the beam radius at different positions along the optical axis in means of the function *Waist fit*. Additionally, the influence of different optical elements, such as lenses, mirrors and dielectric slabs, can be observed by simply placing them at a position along the optical axis.

4 Experimental Results

This chapter presents the relevant experimental results derived during the execution of this thesis. For both used lasers, the beam is characterised utilising the techniques described in section 3.3. To assess the optical power coupled into a waveguide, the efficiency of the used components is measured in means of a power measurement at different spots along the beam path. A derived technique of Alignment for coupling into a waveguide is presented. Using this technique, both used lasers are coupled to waveguides of different properties. For each laser, the influence of the width of the waveguide and the polarisation of the coupled light on the coupling efficiency is studied qualitatively. A method for coupling out of the waveguide is described. Finally, a measurement of the transmitted power through a waveguide is performed.

4.1 Beam Characterisation

4.1.1 Characterisation of the Laser at 405nm Wavelength

The fiber-coupled laser is operated with a collimator, that, according to the manufacturer, corresponds to a waist radius of 375μm. As the used collimator was poorly collimated at the time of measurement, it was adjusted by hand first. This process is extremely delicate and error prone. Hence, the adjusted collimator will correspond to an output beam deviating from the manufacturers specifications.
The profile of the beam is imaged and the intensity distribution along the horizontal and vertical direction is plotted in order to estimate the deviation from a theoretical Gaussian beam. As the single-mode fiber carries only the fundamental mode of the fiber-coupled laser diode, a profile as close as possible to an ideal Gaussian distribution is expected. Figures 4.2 and 4.1 show the obtained results.
The beam exhibits a profile according to an almost circularly symmetrical Gaussian distribution. However, a slightly larger extent of the cross-section can be seen in the vertical direction than in the horizontal direction. Additionally, the spot with the maximum intensity deviates slightly from the beam centre. The plot of the intensity distribution shows a continuous progression with only a few indents at higher intensities along both directions. The walk-off of the point of maximum intensity from the centre is visible. The small deviation from a perfect circularly symmetric

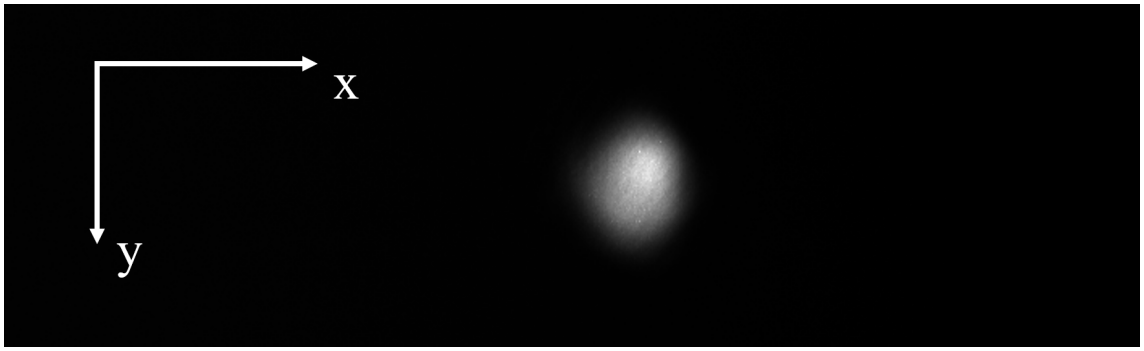

Figure 4.1: Beam profile of the laser at 405nm wavelength.

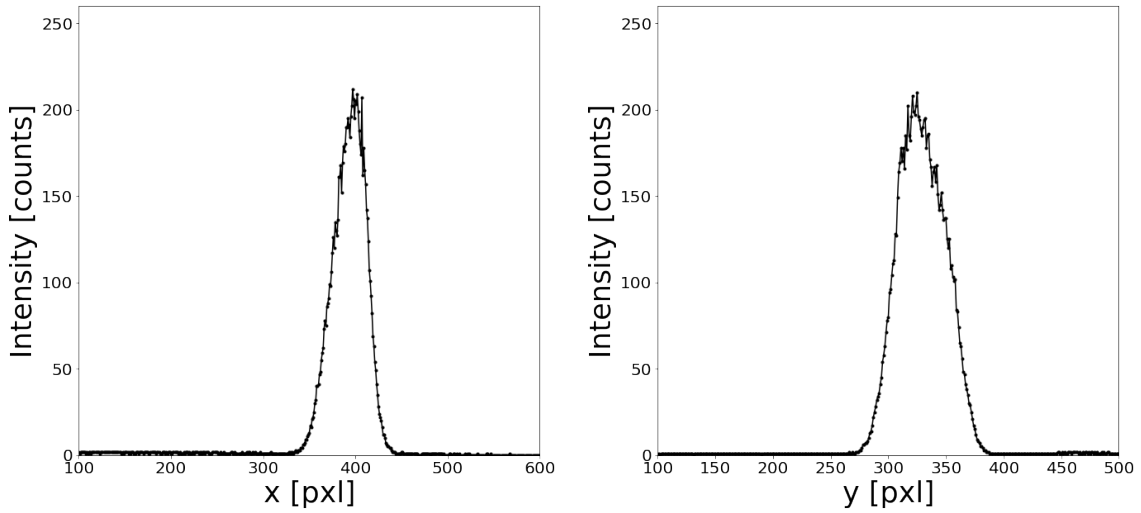

Figure 4.2: Intensity distribution of the laser at 405nm wavelength corresponding to *Left:* the horizontal direction; *Right:* the vertical direction.

beam can be attributed to the by-hand adjusted collimator or the influence of the beamsplitters, used to dim the beam intensity. In the following, an M^2 factor of approximately one is assumed due to the negligible deviation from a Gaussian beam. The knife-edge method is performed for ten different positions of the knife-edge, according to section 3.3. A lens of the focal length $f = 150mm$ is placed in the beam path. For every position of the knife-edge, a fit of the measured transmitted power is performed according to equation 3.2, to determine the corresponding beam radius. As an example, figure 4.3 shows one of the fits. The error for the measured power is calculated from the inaccuracy of the power head and the power meter console and a reading inaccuracy. The error for the measured position corresponds to a reading inaccuracy.

The measured waist radii are used to simulate the beam in means of the software

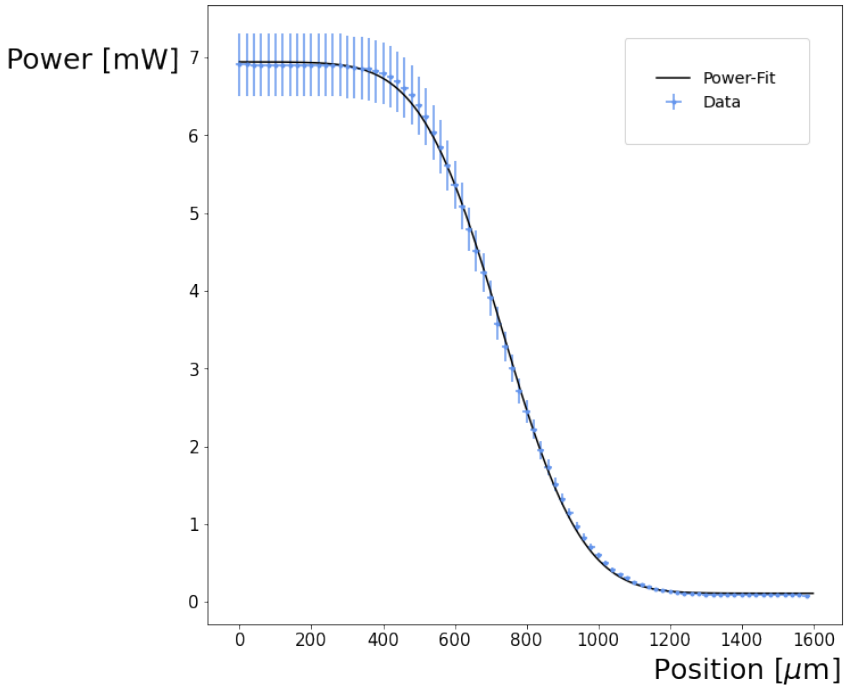

Figure 4.3: Fit of the transmitted power, corresponding to a radius of W = (353 ± 8)μm.

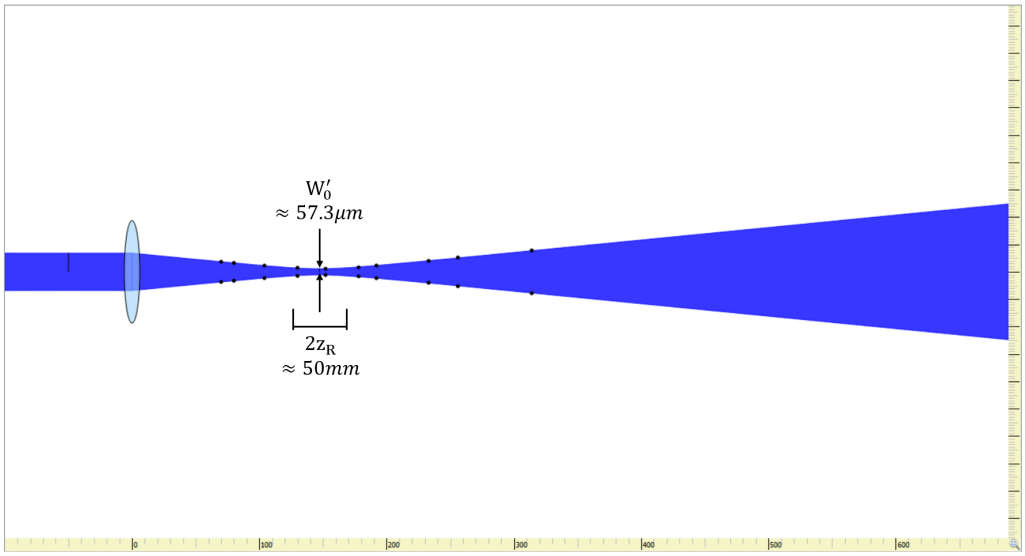

Figure 4.4: Simulation of the laser beam at 405nm wavelength, with the measured beam radii indicated as black dots.

GaussianBeam, which calculates the waist radius and position. Figure 4.4 shows the simulated beam, with the measured beam radii indicated as black dots. The

following result is obtained for the waist radius and position

$$\begin{aligned} W_0 &= (341 \pm 6)\mu m \\ s &= (147 \pm 28)mm \\ M^2 &\approx 1\,, \end{aligned}$$

corresponding to a divergence of $0.378mrad$ of the output beam.
As predicted, the measured waist radius deviates significantly from the manufacturers specification by 5.7σ, due to the process of adjusting the collimator by hand.

4.1.2 Characterisation of the Laser at 317nm Wavelength

To estimate the quality of the laser beam at 317nm wavelength, the profile of the

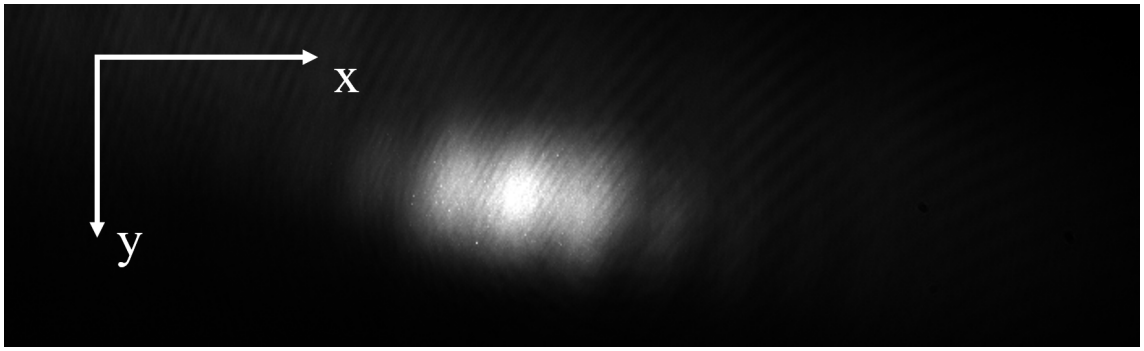

Figure 4.5: Beam profile of the laser at 317nm wavelength.

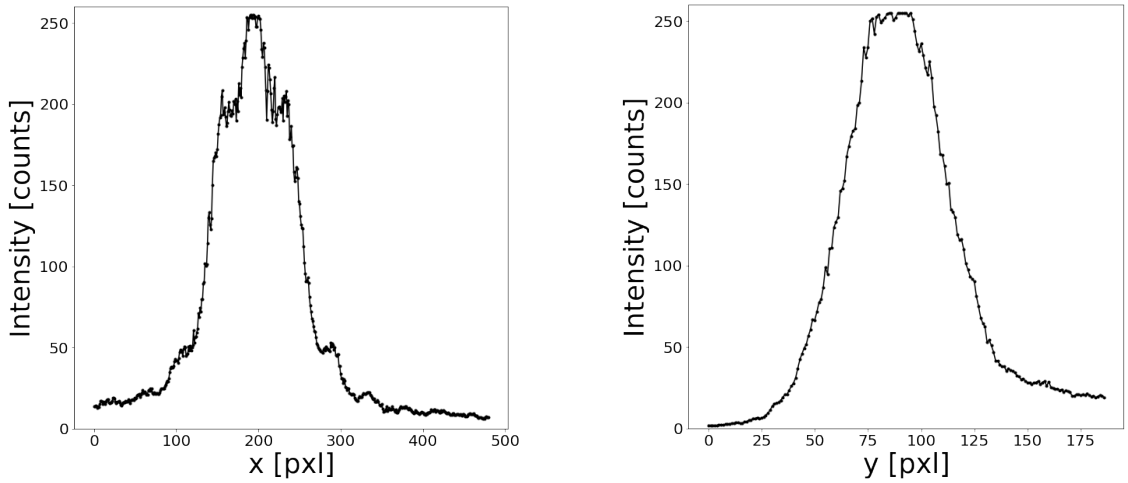

Figure 4.6: Intensity distribution of the laser at 317nm wavelength corresponding to *Left:* the horizontal direction; *Right:* the vertical direction.

beam is imaged and the intensity distribution along the horizontal and vertical direction is plotted. Figures 4.6 and 4.5 show the obtained results.
A beam profile according to an elliptical shaped Gaussian distribution is visible. The profile is distorted by an interference phenomenon, occurring within the laser module. In the vertical direction, many indents are visible throughout the distribution. Additionally, the intensity maximum indicates a plateau-like area. As the Intensity distribution in both, the vertical and horizontal direction, deviates significantly from a Gaussian distribution, a M^2 factor greater than one will be assumed in the following.
The knife-edge method is performed, for ten different positions of the knife-edge

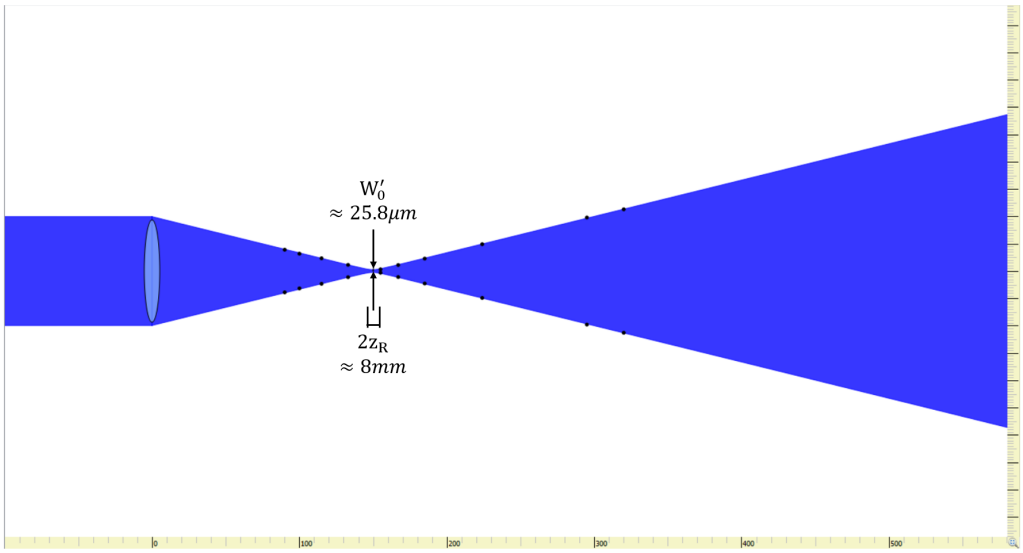

Figure 4.7: Simulation of the laser beam at 317nm wavelength, with the measured beam radii indicated as black dots.

before and after the waist of the focused beam. Again, a lens of the focal length $f = 150.0mm$ is used to focus the beam. The measured radii correspond to the horizontal expansion of the imaged beam profile.
The beam is simulated in means of the simulation software GaussianBeam. Figure 4.7 shows the simulated beam, including the measured beam radii. From the simulation, the waist radius and position and the M^2 factor of the laser result in

$$\begin{aligned} W_0 &= (996 \pm 10)\mu m \\ s &= (0.149 \pm 0.010)m \\ M^2 &\approx 1.7\,, \end{aligned}$$

corresponding to a divergence of $0.172mrad$.

4.2 Efficiency of the used Components

A small fraction of power is lost at every optical component, due to absorption at the material and impurities of the optics. In order to quantify the amount of power coupled into a waveguide and to identify components causing significantly high losses, the optical power is measured in means of a free-space power meter

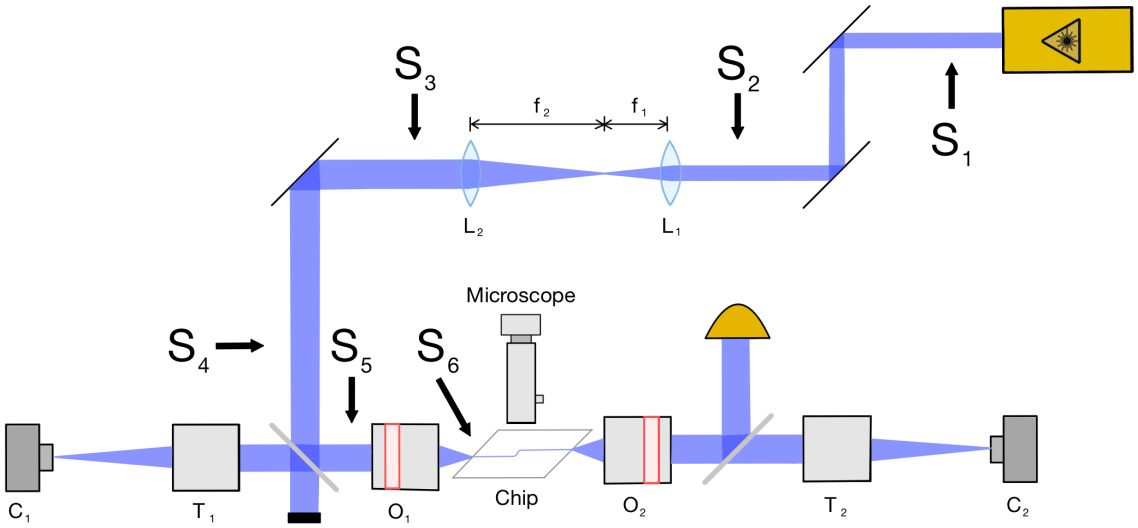

Figure 4.8: Setup for the power measurement at the spots S_i.

at the spots indicated in figure 4.8. Table 4.1 shows the obtained results for the background corrected power measurements alongside the corresponding efficiency η at the spot and the total efficiency of the setup η_{total} until the spot S_i.
According to the manufacturers specifications (section 3.2), the setup should be providing a total efficiency of

$$\begin{aligned} 405nm: &\quad \eta_{theo} = 24.0\% \\ 317nm: &\quad \eta_{theo} = 21.2\% \,. \end{aligned}$$

In a measurement, the setup provides a total efficiency of 18.9% at 405nm wavelength and 26.6% at 317nm wavelength until the spot S_6. Contrary to the expectation, the measured efficiency is higher at the shorter wavelength, for which it exceeds the manufacturers specification. When comparing the measured values for the efficien-

Wavelength	Spot	Power [mW]	η [%]	η_{total} [%]
405nm	S_1	8.766	-	100
	S_2	7.861	89.7	89.7
	S_3	7.603	96.7	86.7
	S_4	7.005	92.1	79.9
	S_5	4.283	61.1	48.9
	S_6	1.660	38.8	18.9
317nm	S_1	10.58	-	100
	S_2	6.307	59.6	59.6
	S_3	5.919	93.8	55.9
	S_4	4.734	80.0	44.7
	S_5	3.300	69.7	31.1
	S_6	2.814	85.3	26.6

Table 4.1: Power measurement and corresponding efficiency at different spots in the setup.

cies at different spots η to the theoretical achievable efficiencies according to the manufacturer, several aspects are conspicuous.

At 405nm wavelength the measured efficiency is strictly higher than the theoretical efficiency for the spots S_1 to S_5. For example, the two lenses forming the Kepler telescope should be transmitting $(96\%)^2 \approx 92.2\%$ of the incident beam. However, the measurement reveals a transmittance of 96.7%. On the contrary, the objective has a transmittance of 38.8% instead of the specified 67% of the incident beam. In total, the measured efficiency is lower than specified at this wavelength, due to the high absorption at the objective.

At 317nm wavelength, the measured efficiency at spot S_2 is significantly lower than specified. Four mirrors were used for correcting the height and direction of the beam, reflecting 59.4% of the incident beam, instead of the specified $(95\%)^4 \approx 74.8\%$. On the contrary, the beamsplitter and the objective both provide a higher efficiency than specified. Hence, in total the efficiency is notably higher than predicted. A possible reason for the high transmission of this laser beam at the objective, is its elliptical shaped beam profile. As the beam was expanded, so that the larger beam radius matched the required entrance beam diameter of the objective, all of the power in the shorter direction of the beam enters the objective. However, the transverse distribution can cause aberrations at the objective. At the beamsplitter a not perfectly unpolarised beam can cause a deviation from the specified splitting ratio. As the aim is to achieve the highest possible efficiency for the laser at 317nm wavelength, no components were exchanged.

4.3 Coupling into the Waveguide

4.3.1 Technique of Alignment

To align the waveguides facet with the objective, the chip is mounted on a motorised translation stage, allowing movements along three axes, in combination with a motorised rotation stage. In the following explanation of the alignment for coupling

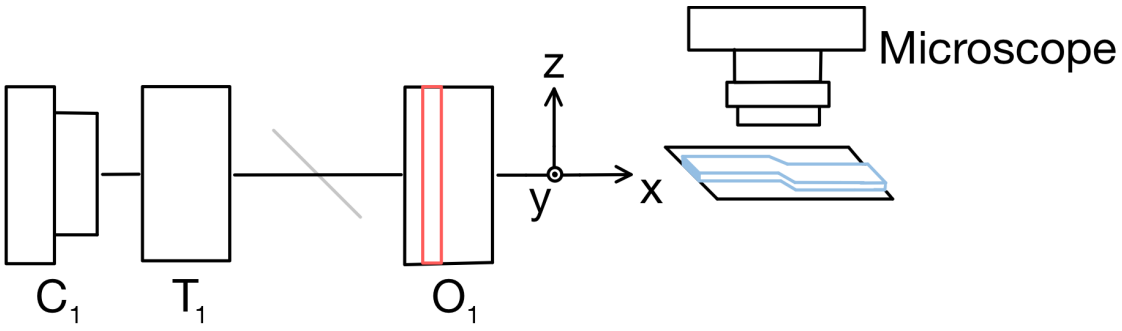

Figure 4.9: Setup for the Alignment for coupling into a waveguide.

into the waveguide, a coordinate system as indicated in figure 4.9 is used. When referring to the monitoring system, the *camera* C_1 refers to the setup monitoring the reflections from the side surface of the chip and the *microscope* refers to the setup monitoring the top surface of the chip.

First, a starting position for the alignment of the waveguides facet with the optical axis is set. The chip is mounted with the waveguide facets facing the objective, approximately at the height of the optical axis. By moving the chip along the x axis, the facet-objective distance is adjusted to approximately match the working distance of the objective. At this point, the first reflections of the beam from the side surface of the chip should become visible on camera C_1. If this is not the case, the height of the chip should be adjusted. Once reflections are visible, a suitable starting position for the alignment is reached.

Second, the position along the x axis is adjusted precisely. For this sake, the reflections visible on camera C_1 are used as feedback. By altering the x position, the side surface of the chip is moved towards the waist of the focused beam, at which the observed reflections are of minimal size. Hence, the size of the reflections serves as an indicator for the correct position along the x axis. Close to the waist, it is often the case that a diffraction pattern appears, as shown in figure 4.10 on the left. This pattern can also be used as an indicator. The correct x position is found, once the smallest possible spot size of the reflections is reached and, if it is visible, the

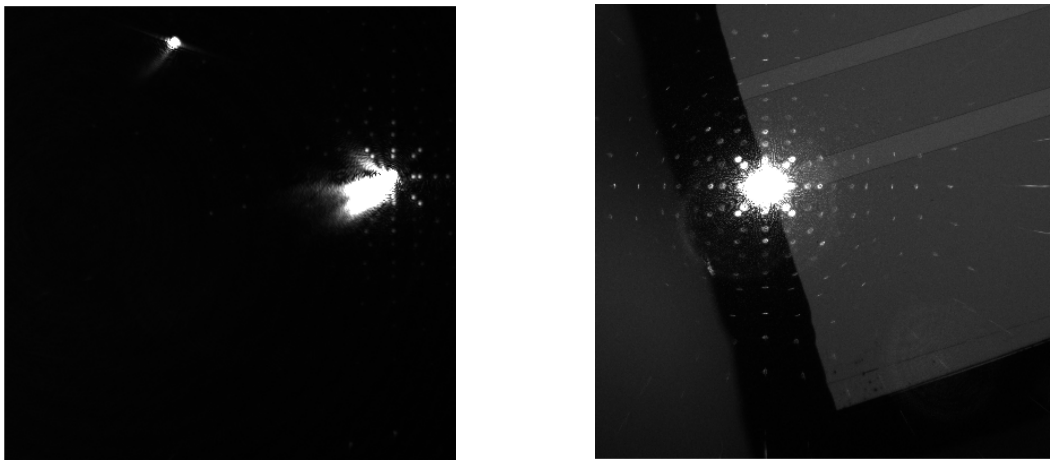

Figure 4.10: x Position adjusted correctly, monitoring with *Left*: the camera C_1; *Right*: the microscope.

diffraction pattern is in focus on the camera C_1.
Third, the facet of the waveguide is aligned with the optical axis. For this sake, the chip is lowered along the z direction, until a reflection of the laser beam from the upper edge of the chip is visible through the microscope. For a properly adjusted

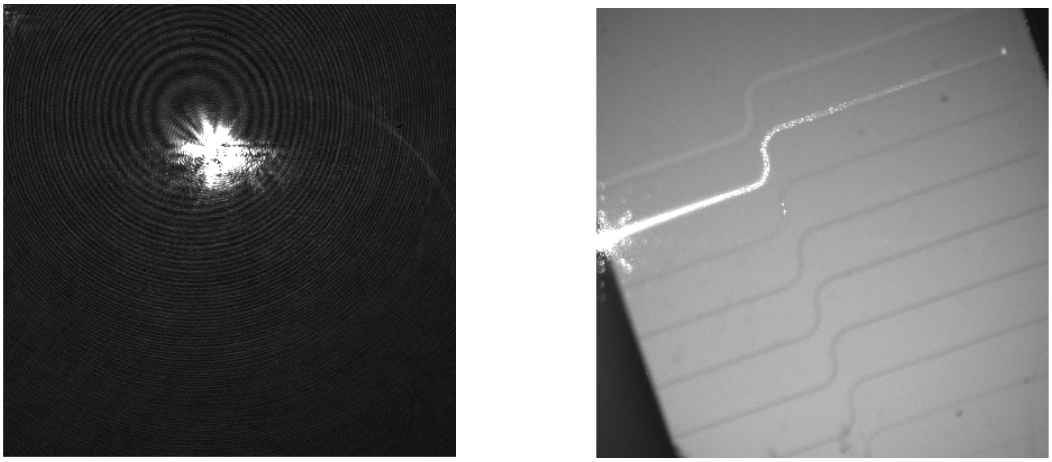

Figure 4.11: Silicon Nitride waveguide of 50μm width and 200nm height, coupled at 405nm wavelength, monitoring with *Left*: the camera C_1; *Right*: the microscope.

x position, most likely a diffraction pattern, similar to figure 4.10 on the right, will appear. The chip can now be moved along the y direction, until this reflection coincides with the position of the aspired waveguide. Subsequently, a small step size along the z axis is chosen, to further lower the chip. Once, the z position is approximately correct, the first losses within the waveguide should be visible through the microscope.

Finally, once losses are visible the smallest possible step size is chosen for every degree of freedom. Based on the losses observed through the microscope, the position of the chip is adjusted until the observed losses are maximum. As an example, figure 4.11 shows a coupled waveguide.

4.3.2 Coupling at 405nm Wavelength

For first tests, the fiber-coupled laser at 405nm wavelength is coupled into multiple waveguides of different properties. As previous sections have shown, this laser exhibits a high quality output beam as close as possible to a circularly symmetric Gaussian. Hence, a low level of aberration is expected at the objective. The spot size achievable in means of the objective is 0.9μm. After beam shaping, 18.9% of the output power can be coupled into the waveguide.

Polarisation of the coupled Light

As explained in section 2.2, a mode of the waveguide is excited by the coupled light if the polarisation of the light matches that of the mode. Hence, the influence of the

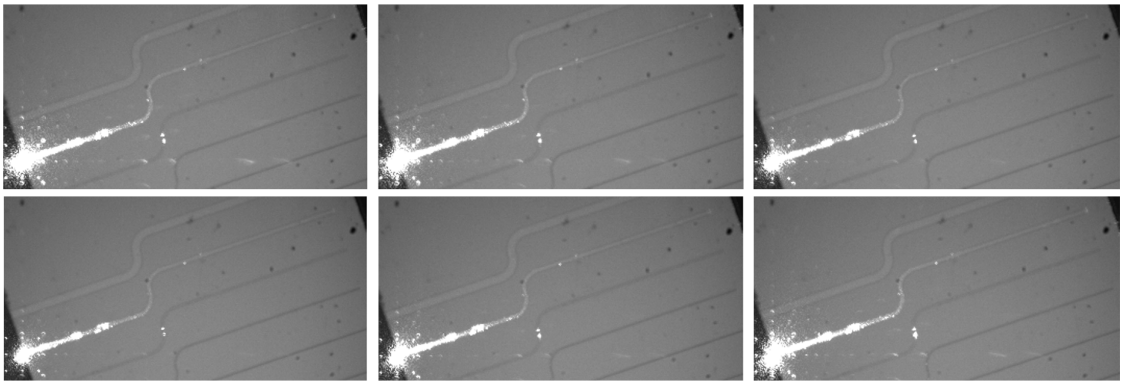

Figure 4.12: Silicon Nitride waveguide of 50μm width and 200nm height, coupled at 405nm wavelength of varying polarisation.

polarisation of the coupled light on the coupling efficiency is examined by altering the polarisation in means of a half-waveplate. If the polarisation has a notable influence on the coupling efficiency, more or less losses should become visible in means of the microscope monitoring the top surface of the chip. Figures 4.12 and 4.13 show the top surface of a coupled Silicon Nitride and an Aluminium Gallium Nitride waveguide for 6 different settings of the waveplate between 0° and 90°.
The images suggest a negligible influence of the polarisation of the coupled light on the coupling efficiency for both waveguide materials. However, the polarisation

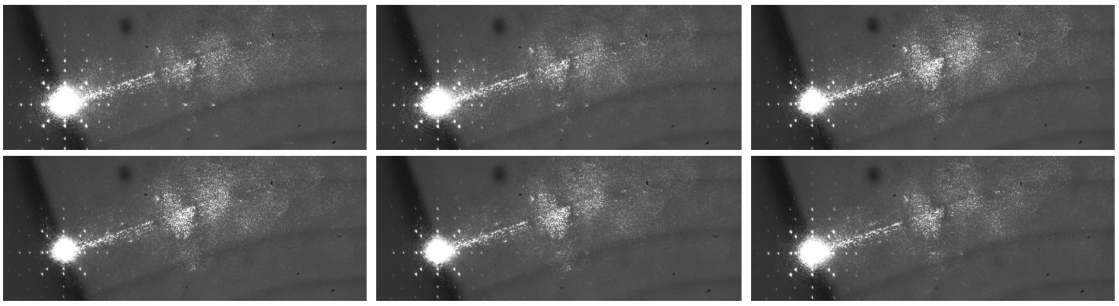

Figure 4.13: Aluminium Gallium Nitride waveguide of 5μm width and 300nm height, coupled at 405nm wavelength of varying polarisation.

does have an influence on the reflectance of the used beamsplitter, as mentioned in section 3.2. For the following measurements the waveplate is adjusted, so that a maximum power is reflected from the beamsplitter towards the objective.

Width of the coupled Waveguide

A functional setup should enable to characterise a wide range of different waveguide geometries. However, the spot size achievable in means of the objective results in

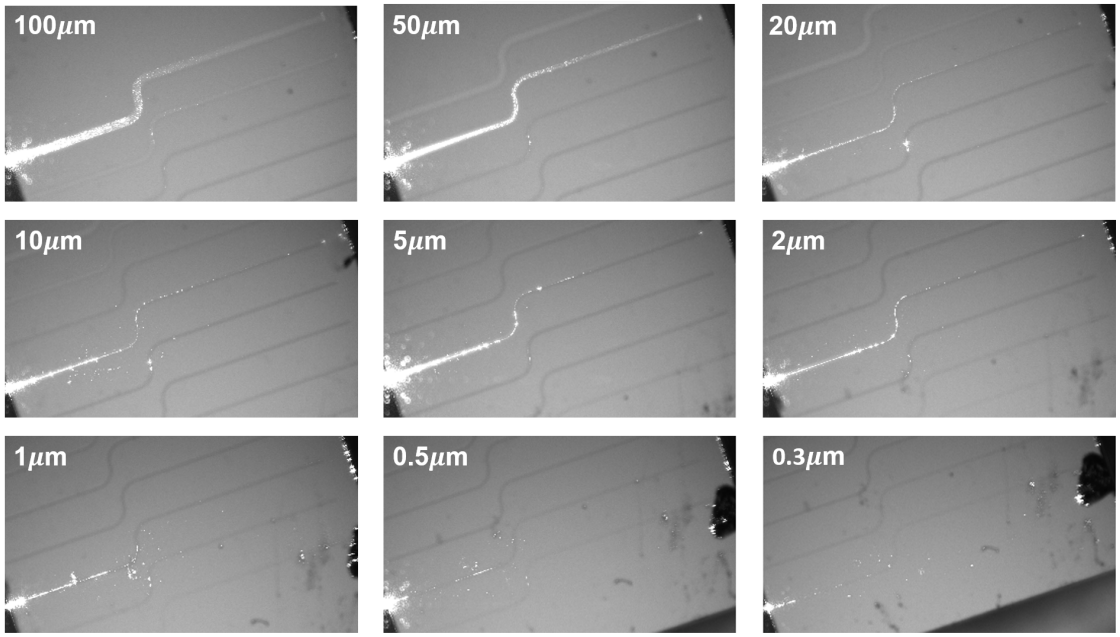

Figure 4.14: Silicon Nitride waveguides of varying width between 100μm and 0.3μm and 200nm height, coupled at 405nm wavelength.

a low coupling efficiency for smaller waveguide facets. In order to estimate which waveguide width still enables a sufficient coupling efficiency, the beam is coupled

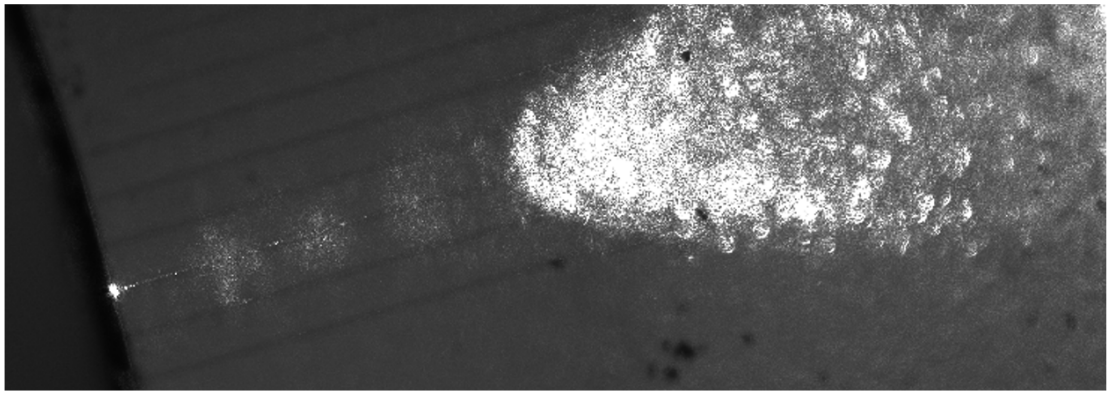

Figure 4.15: Aluminium Gallium Nitride waveguides of 5μm width and 300nm height, coupled at 405nm wavelength.

into waveguides of varying width. The losses within the waveguide are observed qualitatively in means of the microscope monitoring the top surface of the chip. Figures 4.14 and 4.15 show Silicon Nitride waveguides of varying width, coupled with the same output power of the laser and the same integration time of the used camera and a coupled Aluminium Gallium Nitride waveguide.
For Silicon Nitride the images show that light was successfully coupled into every observed waveguide. However, the coupling efficiency varies with the width. A high efficiency is observed at widths between 100μm and 2μm. The three narrowest waveguides show significantly less losses, corresponding to less light coupled into the waveguides.
Light was only coupled to one Aluminium Gallium Nitride waveguide. As depicted in figure 4.15, for this material a major part of the coupled light is diffracted into the cladding. Hence, it is not recognisable, whether light transmits through the S bend or if it is completely diffracted into the cladding.
It should be noted here that the coupling efficiency is highly dependent on the quality of the facet. A successful coupling to a specific waveguide, does not imply that light can be coupled into a different waveguide of a similar design with the same coupling efficiency. Additionally, impurities within the waveguide can cause a lower transmission through the waveguide.

4.3.3 Coupling at 317nm Wavelength

The aspired wavelength for the proposed setup is 316nm. Previous sections have shown that the laser at 317nm wavelength exhibits a low quality output beam with a profile according to an elliptical shaped Gaussian beam, distorted by an interference phenomenon. The transverse distribution of the beam can cause aberrations at the objective. The spot size achievable in means of the objective is 1.2μm, when considering the measured M^2 factor. After beam shaping, 26.6% of the output power can be coupled into the waveguide. During the execution, this laser was only successfully coupled to Silicon Nitride waveguides.

Polarisation of the coupled Light

To observe the influence of the polarisation of the coupled light on the coupling efficiency, the beam is coupled into a Silicon Nitride waveguide and the polarisation is varied in means of a half-waveplate. Figure 4.16 displays the top surface of a

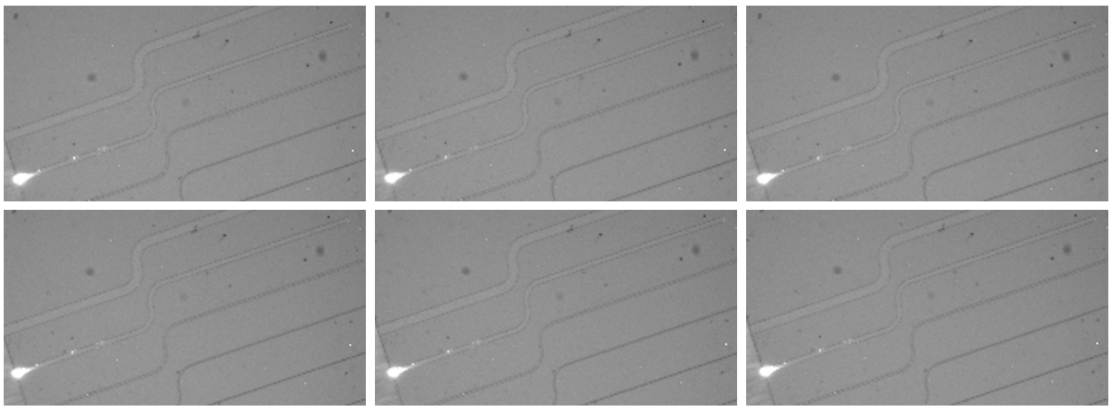

Figure 4.16: Silicon Nitride waveguide of 50μm width and 200nm height, coupled at 317nm wavelength of varying polarisation.

Silicon Nitride waveguide, coupled at 317nm wavelength for 6 different settings of the waveplate between 0° and 90°.

The images, suggest a negligible influence of the polarisation of the coupled light on the coupling efficiency. Hence, the waveplate is adjusted, so that a maximum power is reflected from the beamsplitter towards the objective for the following measurements.

Width of the coupled Waveguide

For this laser, again the influence of the waveguide width on the coupling efficiency is examined. Figure 4.17 shows Silicon Nitride waveguides of varying width, coupled with approximately the same output power of the laser and the same integration time of the used camera.

The images show, that light has been coupled into every waveguide. However, almost

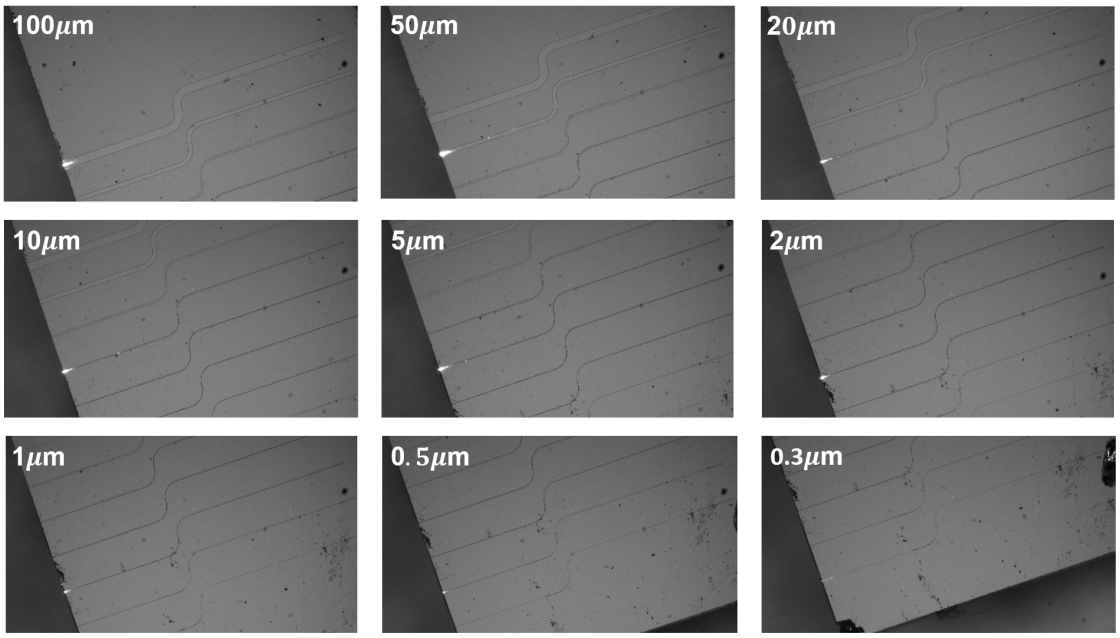

Figure 4.17: Silicon Nitride waveguides of varying width between 100μm and 0.3μm and 200nm height, coupled at 317nm wavelength.

no losses within the waveguides are visible at the top surface of the chip. As of now, it is unclear whether the coupling efficiency is generally exceptionally low for this laser beam or whether there are not enough losses behind the facet to be observed in means of the microscope. Hence, at this wavelength the successful coupling can solely be assessed by observing the transmitted power through the waveguide.

4.4 Coupling out of the Waveguide

4.4.1 Technique of Alignment

The light transmitted through a waveguide is collected and collimated in means of an infinity-corrected objective. As described in section 3.1, this objective is part of an infinity-corrected microscope system containing a beamsplitter. In order to

align this setup with the back facet of the coupled waveguide, from which light is escaping, it is mounted on a translation stage allowing movements along three axes. In general, even for a high coupling efficiency there is stray light at the back edge of the chip, as shown in figure 4.18 on the left. When aligning the objective with

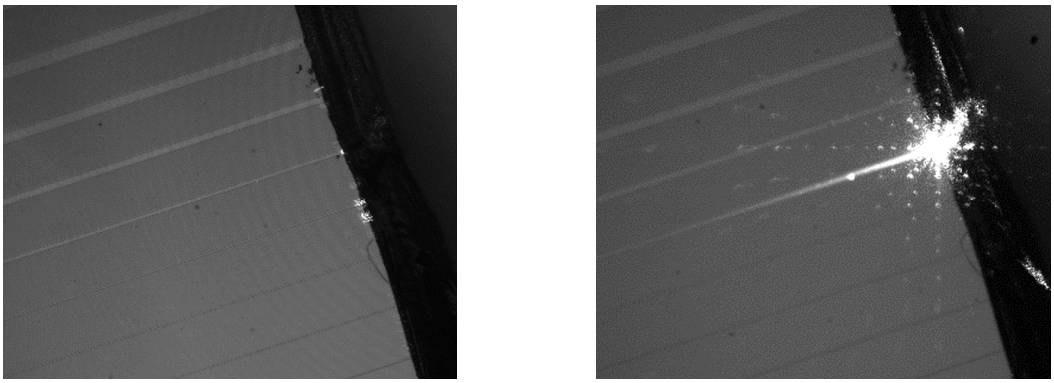

Figure 4.18: *Left*: Stray light at the edge of the chip for a Silicon Nitride waveguide of 5μm width and 200nm height, coupled at 405nm wavelength; *Right*: The same waveguide coupled at the back end at 405nm wavelength.

the back facet, the stray light can be mistaken for transmitted light through the waveguide. To circumvent this problem, the microscope setup is aligned with the aspired back facet of the waveguide by coupling light into this facet through the objective collimating the escaping beam. For this purpose, a collimator guides the light of the fiber-coupled laser diode towards the beamsplitter within the microscope setup. This beamsplitter reflects the beam towards the objective for coupling out of the waveguide. The proposed technique of alignment for coupling into a waveguide (section 4.3.1) is performed with the three axes of the translation stages of the microscope setup as the degrees of freedom. Once light has been coupled into the back end of the aspired waveguide, the correct position for coupling out of the waveguide is found. Figure 4.18 shows a waveguide, coupled at the back end.

4.4.2 Transmission Measurement

A measurement of the transmitted power of the fiber-coupled laser at 405nm wavelength is performed for a Silicon Nitride waveguide of 20μm width and 200nm height. The waveguide has a length of approximately 1cm. The coupled laser has already been successfully coupled into a waveguide of the similar design and material on another chip. Light is coupled into the waveguide according to section 4.3.1. Once the position of the chip allows for a sufficient coupling efficiency, light is coupled

into the back facet of the same waveguide, according to the previous section 4.4.1. Figure 4.19 shows the top surface of the Silicon Nitride waveguide, coupled from

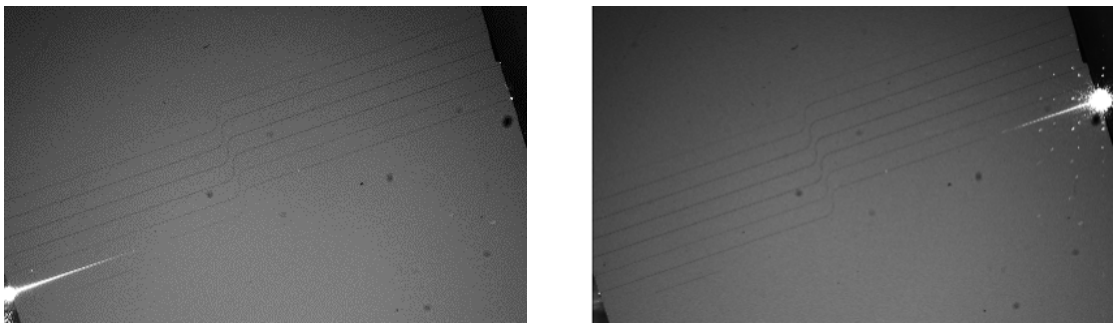

Figure 4.19: Silicon Nitride waveguide of 20μm width and 200nm height, coupled at 405nm wavelength *Left*: to the front facet; *Right*: to the back facet.

both sides at 405nm wavelength. Once the aspired position of both, the chip and the microscope setup for coupling out of the chip is reached, the transmitted power through the waveguide is measured.
The waveguide is coupled with an output power of the laser at 405nm wavelength of 8.681mW, corresponding to a power of 1.641mW of the focused beam, which is theoretically coupled into the waveguide. The transmitted power P_T is measured in means of a power meter, located in the reflected beam path from the beamsplitter. The measurement reveals a transmitted power of

$$P_T = (3.730 \pm 0.010)\mu W \tag{4.1}$$

$$P_0 = (0.126 \pm 0.010)\mu W\,, \tag{4.2}$$

where P_0 denotes the background power. The errors correspond to fluctuations of the measured power.
Before the transmitted light meets the power meter, it is transmitted through an objective and reflected from a beamsplitter, which reflects 90% of the beam. At both components, a fraction of the transmitted power is lost. To determine the true transmitted power, the average transmittance through the objective and the reflectance of the beamsplitter according to the manufacturers specification is included. Thus, the transmitted power results in

$$P_T = (6.060 \pm 0.010)\mu W\,, \tag{4.3}$$

encompassing the specifications of the optics and the background power. This corresponds to a coupling efficiency of approximately 24dB.
When altering the polarisation of the coupled light in means of a half-waveplate, the transmitted power changes by approximately 5%. This can be attributed to the polarisation dependence of the splitting ratio of the beamsplitter. For the measurement, the waveplate was adjusted, so that the transmitted power is maximum.
It should be noted here that the size of the entrance pupil of the objective precludes the capture of all of the transmitted light. Accordingly, this measurement gives only an indication of the actual transmitted power.

5 Conclusion and Outlook

In this thesis a free-space optical setup was built for the characterisation of integrated optical modulator circuits. The aspired wavelength lies in the UV range at 316nm. A suitable waveguide material for this wavelength is Aluminium Gallium Nitride. The setup was built with a free-space laser at a wavelength of 317nm, close to the aspired wavelength. A fiber-coupled laser at a wavelength of 405nm was used for the coarse alignment of the setup and first tests. This laser comes close to the aspired UV spectral range and bears advantages regarding the beam quality. The primary function of this setup is the coupling of a free-space beam into and out of an integrated waveguide.

Both used lasers were characterised. First, the beam profile was imaged and the intensity distribution was observed. As the laser at 405nm is fiber-coupled, it exhibits an almost circularly symmetric beam profile, corresponding to a high quality output beam. The laser at 317nm wavelength has an elliptical shaped beam profile, distorted by an interference phenomenon, corresponding to a low quality output beam. Subsequently, the waist radius, waist position and M^2 factor was determined for both lasers, which determine the beam propagation in free-space. The accuracy of the obtained results could have been improved by including additional measurement points by means of the knife-edge method. The transverse distribution of the beam is crucial for coupling to a waveguide, as the used objective works with the lowest level of aberration for a circularly symmetric transverse distribution, corresponding to a radius of 1.7mm. Both lasers are expanded to the correct waist radius in means of a Kepler telescope within the accuracy of the measured propagation determining parameters. However, as the laser at 317nm wavelength exhibits an elliptical shaped distribution, distorted by an interference phenomenon, aberrations can occur for this laser. For the laser at 405nm wavelength, a low level of aberration is expected.

The efficiency of the used components was determined in means of a power measurement at different spots throughout the beam path. This measurement gives insights on optics deviating significantly from the manufacturers specifications and the amount of power coupled into the waveguide. Both of the measured efficiencies differ from the specifications. Contrary to expectations, a higher efficiency of the components was observed for the shorter wavelength of 317nm with 26.6% in comparison to the laser at 405nm wavelength with 18.9%. At 317nm wavelength, the measurement even exceeds the specified achievable efficiency. Possible reasons for the deviations were analysed. As a high efficiency of the components at this wavelength is beneficial for the setup, no components were exchanged.
A derived technique for coupling the free-space beam into a waveguide was presented. Using this technique both lasers were coupled to different waveguide designs and the influence of the polarisation and the waveguide width on the coupling efficiency was studied qualitatively. Measurements revealed a negligible influence of the polarisation of the coupled lasers on the coupling efficiency. Both lasers were coupled to Silicon Nitride waveguides of a minimum width of 0.3μm. At 405nm wavelength, losses were observed throughout the waveguide. However, at 317nm wavelength losses were only observed at the coupled end of the waveguide. Successful coupling can be verified by measuring the transmitted power through a waveguide. Light of 405nm wavelength was also coupled to an Aluminium Gallium Nitride waveguide. However, the used chip exhibits heavy diffraction of the coupled light into the cladding and low quality facets, precluding further examinations.
The transmitted light through a waveguide is collected and collimated in means of an infinity-corrected objective. A derived technique for aligning this objective with the back end of the waveguide was presented. Using this technique, the transmitted power of the laser at 405nm wavelength through a Silicon Nitride waveguide of 20μm width and 200nm height was measured. A coupling efficiency of approximately 24dB was revealed for the examined waveguide. The negligible influence of the polarisation of the coupled light on the coupling efficiency was verified. At the observed chip, the other waveguides correspond to facets of low quality, which excludes a descriptive measurement of the coupling efficiency for different waveguide widths. Additionally, as the laser at 317nm wavelength had a technical defect at the time of measurement, no transmission measurement was performed for the aspired wavelength. The heavy diffraction into the cladding at the Aluminium Gallium Nitride waveguides exclude a measurement of the transmitted power for this waveguide material.

Before the main objective of this setup is realised, there are still a number of milestones to overcome.
As of now, it is possible to evaluate different waveguide designs and techniques of fabrication. By performing different measurements, it was already identified, that the current design and fabrication of the Aluminium Gallium Nitride waveguides is in need of improvement. Additionally, a successful technique of fabrication for the Silicon Nitride waveguides was observed.
Improvements to the setup include, switching both stages responsible for the alignment to motorised stages with a smaller possible step size and a higher accuracy. Additionally, the microscope setup for coupling out of the waveguide should be mounted on a rotation stage to collect the transmitted beam with a higher precision. Furthermore, the beam of the laser at 317nm wavelength can be shaped to a circularly symmetric shape to reduce aberrations at the objective. At the time of measurement, a technical defect of the laser at 317nm wavelength resulted in a low output power of this laser. By fixing this defect, further measurements utilising the aspired wavelength of 317nm will be possible. Thus, the transmitted power of this laser through different waveguide designs will be measured. Furthermore, by utilising a new technique of fabrication for Aluminium Gallium Nitride waveguides, both lasers will be coupled to the aspired waveguide material and a measurement of the transmitted power will be performed.

Bibliography

[1] Javier Alda. "Laser and Gaussian beam propagation and transformation". In: *Encyclopedia of optical engineering* 999 (2003), pp. 1013–1013.

[2] Massimo Bertaccini. *Cryptography Algorithms*. Packt Publishing, 2022.

[3] Hans Joachim Eichler, Jürgen Eichler, and Oliver Lux. *Lasers. Basics, Advances and Applications*. Springer Cham, 2018. ISBN: 978-3-319-99893-0. DOI: https://doi.org/10.1007/978-3-319-99895-4.

[4] Thomas F Gallagher. "Rydberg atoms". In: *Reports on Progress in Physics* 51.2 (1988), p. 143.

[5] Sara Gamble. *Quantum Computing. What It Is, Why We Want It, and How We're Trying to Get It*. National Academy of Engineering, 2019. DOI: https://www.ncbi.nlm.nih.gov/books/NBK538701/.

[6] Christoph Greb. "Infinity Optical Systems: From infinity optics to the infinity port". In: *Optik & Photonik* 11.1 (2016), pp. 34–37.

[7] Laser Components Group. *Optical Fibers for UV Applications*. URL: https://www.lasercomponents.com/de-en/news/optical-fibers-for-uv-applications/. (Accessed: 02.09.2023).

[8] Ginés Lifante. *Integrated Photonics. Fundamentals*. John Wiley & Sons Ltd, 2003. ISBN: 0-470-84868-5.

[9] *MUNICQ-ATOMS. Neutral Atom based Quantum Computing Demonstrator*. URL: https://muniqc-atoms.munich-quantum-valley.de/about. (Accessed: 16.08.2023).

[10] Richard jr. Osgood and Xiang Meng. *Principles of Photonic Integrated Circuits. Materials, Device Physics, Guided Wave Design*. Springer Cham, 2021. ISBN: 978-3-030-65193-0. DOI: https://doi.org/10.1007/978-3-030-65193-0.

[11] Stefan Roth and Achim Stahl. *Optik. Experimentalphysik – anschaulich erklärt*. Springer Spektrum Berlin, Heidelberg, 2019. ISBN: 978-3-662-59336-3. DOI: https://doi.org/10.1007/978-3-662-59337-0.

[12] Bahaa E. A. Saleh and Malvin Carl Teich. *Fundamentals of Photonics*. John Wiley & Sons, 1991. ISBN: 0-471-2-1374-8.

[13] Prof. Dr. Florian Scheck. *Klassische Feldtheorie - Von Elektrodynamik, nicht-Abelschen Eichtheorien und Gravitation*. Springer-Verlag Berlin Heidelberg, 2010. ISBN: 978-3-642-03961-4.

[14] Hiu Yung Wong. *Introduction to Quantum Computing. From a Layperson to a Programmer in 30 Steps*. Springer International Publishing AG, 2022. ISBN: 9783030983390.

[15] C Yeh. "Optical waveguide theory". In: *IEEE Transactions on Circuits and Systems* 26.12 (1979), pp. 1011–1019.

Acknowledgements

First and foremost I am deeply grateful to Professor Wolfram Pernice for giving me the opportunity to work in his research team for my thesis and expand my knowledge about free-space optics. I am also very thankful to Professor Lauriane Chomaz for agreeing to be my second examiner for this thesis.

My gratitude exceeds to Philipp Schultzen and Klara Maria Meyer-Herrmann for providing me with valuable knowledge, guiding me throughout this thesis and fabricating chips for testing the setup. Without their help this thesis would not have been possible.

Finally, I want to thank every member of the Neuromorphic Quantumphotonics team, for the professional feedback during group meetings and emotional support.

Erklärung

Ich versichere, dass ich diese Arbeit selbstständig verfasst und keine anderen als die angegebenen Quellen und Hilfsmittel benutzt habe.

Heidelberg, den 22. September 2023

Nisa Kassandra Wöll